Field measurement and prediction of drag in a planted Rhizophora mangrove forest

Yoshikai Masaya[1], Nakamura Takashi[1], Bautista Dominic M[2], Herrera Eugene C[2], Baloloy Alvin[2], Suwa Rempei[3], Basina Ryan[4], Primavera-Tirol Yasmin H[4], Blanco Ariel[5], and Nadaoka Kazuo[1]

[1]Tokyo Institute of Technology
[2]University of the Philippines, Diliman
[3]Japan International Research Center for Agricultural Sciences
[4]Aklan State University
[5]University of the Phili[[ines

November 16, 2022

Abstract

Mangrove forests with complex root systems contribute to increased coastal protection through drag effects. Previous flume studies proposed a predictive model of drag in Rhizophora mangrove forests based on quadratic drag law. However, its general applicability on mangrove forests in the field has not been tested. To fill this knowledge gap, this study quantified drag in a 17-year-old planted Rhizophora mangrove forest using a comprehensive measurement of hydrodynamics and vegetation morphology. The vegetation projected area density, a, showed an approximate exponential increase towards the bed, mainly due to root branching. This vertical variation led to enhanced vegetation drag per unit water volume relative to velocity with decreasing water depth. Alternatively, the drag per vegetation projected area solely depended on the square of velocity, indicating association with the quadratic drag law. The derived drag coefficient (CD) was 1.0 ± 0.2 for tide-driven currents, consistent with previous flume studies. By using the mean value of derived CD (1.0), it was confirmed that the quadratic drag model expresses well the field-measured drag. We also presented a method for predicting a value for a, another unknown parameter in the drag model, using an empirical Rhizophora root model, and confirmed a successful prediction of a and drag. Therefore, the drag in a Rhizophora mangrove forest can be accurately predicted only using the input parameters of the Rhizophora root model – stem diameter and tree density. This provides insights into effectively implementing the drag model in hydrodynamic models for better representation of mangroves' coastal protection function.

Field measurement and prediction of drag in a planted *Rhizophora* mangrove forest

Masaya Yoshikai[1*], Takashi Nakamura[1], Dominic M. Bautista[2], Eugene C. Herrera[2], Alvin Baloloy[3], Rempei Suwa[4], Ryan Basina[5], Yasmin H. Primavera-Tirol[5], Ariel C. Blanco[3], Kazuo Nadaoka[1]

[1]School of Environment and Society, Tokyo Institute of Technology, O-okayama 2-12-1 W8-13 Meguro, Tokyo 152-8552, Japan

[2]Institute of Civil Engineering, University of the Philippines, Diliman, Quezon City 1101, Philippines

[3]Department of Geodetic Engineering, College of Engineering, University of the Philippines, Diliman, Quezon City 1101, Philippines

[4]Forestry Division, Japan International Research Center for Agricultural Sciences (JIRCAS), 1-1 Ohwashi, Tsukuba, Ibaraki 305-8686, Japan

[5]College of Fisheries and Marine Sciences, Aklan State University, New Washington, Aklan, Philippines

Corresponding author: Masaya Yoshikai (yoshikai.m.aa@m.titech.ac.jp)

Key points

- Field-derived drag coefficient of a planted *Rhizophora* mangrove forest was around 1.0, consistent with previous flume studies.
- Quadratic drag model accurately predicted the field-measured drag force exerted in the mangrove forest.
- Drag can be effectively predicted using only stem diameter and tree density by employing an empirical model for *Rhizophora* root morphology.

Abstract

Mangrove forests with complex root systems contribute to increased coastal protection through drag effects. Previous flume studies proposed a predictive model of drag in *Rhizophora* mangrove forests based on quadratic drag law. However, its general applicability on mangrove forests in the field has not been tested. To fill this knowledge gap, this study quantified drag in a 17-year-old planted *Rhizophora* mangrove forest using a comprehensive measurement of hydrodynamics and vegetation morphology. The vegetation projected area density, a, showed an approximate exponential increase towards the bed, mainly due to root branching. This vertical variation led to enhanced vegetation drag per unit water volume relative to velocity with decreasing water depth. Alternatively, the drag per vegetation projected area solely depended on the square of velocity, indicating association with the quadratic drag law. The derived drag coefficient (C_D) was 1.0 ± 0.2 for tide-driven currents, consistent with previous flume studies. By using the mean value of derived C_D (1.0), it was confirmed that the quadratic drag model expresses well the field-measured drag. We also presented a method for predicting a value for a, another unknown parameter in the drag model, using an empirical *Rhizophora* root model, and confirmed a successful prediction of a and drag. Therefore, the drag in a *Rhizophora* mangrove forest can be accurately predicted only using the input parameters of the *Rhizophora* root model – stem diameter and tree density. This provides insights into effectively implementing the drag model in hydrodynamic models for better representation of mangroves' coastal protection function.

Plain Language Summary

Mangrove forests with *Rhizophora* trees that have complex above-ground root systems attenuate flow and wave energy and protect coasts from disasters such as storm surges and high

waves. This drag effect of mangrove forests has been previously examined by flume experiments and characterized with two parameters – drag coefficient and vegetation frontal area. However, field measurements of drag in mangrove forests are limited and it is still unknown whether the insights obtained by flume experiments are applicable to mangrove forests in the field. To fill this knowledge gap, this study quantified drag in a 17-year-old planted *Rhizophora* mangrove forest based on field measurements. We showed that the value of drag coefficient obtained in previous flume studies can be used for drag prediction in mangrove forest examined in this study, suggesting the applicability of the insights from flume experiments to the field. We also showed that the vegetation frontal area – another needed information for drag prediction – can be predicted only using information on stem diameter and tree density using an empirical model for *Rhizophora* root morphology. These results provide a way for effectively predicting drag in *Rhizophora* mangrove forests in the field, thus contributing a better understanding of mangroves' coastal protection function.

Keywords: coastal vegetation; coastal protection; nature-based solution; drag coefficient; root morphology

1. Introduction

Mangroves are one of the coastal vegetation ecosystems that grow in intertidal areas in tropical and subtropical regions (Giri et al., 2011). They are characterized by complicated patterns of above-ground root systems (Ezcurra et al., 2016; Tomlinson, 2016) that substantially attenuate flow and wave energy and provide coastal protection (Furukawa et al., 1997; Horstman et al., 2014; Menéndez et al., 2018, 2020). The significance of mangrove forests in reducing damages by tsunami-induced waves and storm surges through their drag effects has been noted by field, laboratory, and numerical modeling studies (Danielsen et al., 2005; Krauss et al., 2009; Yanagisawa et al., 2010; Zhang et al., 2012; Strusińska-Correia et al., 2013; Maza et al., 2019, 2021; Montgomery et al., 2019; Tomiczek et al., 2020). While the risk of coastal flooding is expected to increase in the future due to increased occurrence of more intense cyclones and sea-level rise (Woodruff et al., 2013), the coastal protection function of mangrove forests is of great interest as a sustainable and cost-effective nature-based solution (Temmerman et al., 2013; Gijsman et al., 2021).

Despite the valuable ecosystem services provided by mangroves, they have declined globally predominantly due to deforestation (Friess et al., 2019). Although the perception of mangroves ecosystem services has encouraged management actions such as protection and restoration, deforestation is still ongoing especially in Southeast Asia (Friess et al., 2020). Rigorous evaluation of the coastal protection function would help in better decision making for facilitating management actions and implementation of nature-based solutions (Menéndez et al., 2018; Gijsman et al., 2021). However, our understanding of the drag effects of mangrove forests remains limited due to the complex architecture of root systems which makes it a challenging task to quantify. Hence, this study aims to quantify mangroves drag from field measurements and contribute to a better understanding of the mangroves' coastal protection function. This study specifically focuses on the drag effects of *Rhizophora* genus which is known to form complicated prop root systems (Ong et al., 2004). It is one of the most dominant mangrove genera in the Asia-Pacific region and is often used for mangrove plantation (Primavera and Esteban, 2008; Friess et al., 2019).

Recently, several studies have conducted flume experiments using model *Rhizophora* trees to characterize the flow and drag in *Rhizophora* mangrove forests (Zhang et al., 2015; Maza et al., 2017; Shan et al., 2019). They showed that the model based on the quadratic drag law with the spatial average of streamwise depth-averaged velocity or channel mean velocity

(U, m s^{-1}) can well express the drag exerted by mangroves (vegetation drag). This can be written in a form of spatial average as (Nepf, 2012; Xu and Nepf, 2021)

$$F_{veg,model} = \frac{1}{2}\frac{C_D}{1-\varphi} AU|U| \quad \text{where} \quad A = \int_0^h a(z)dz \tag{1}$$

where $F_{veg,model}$ is the modeled vegetation drag per bed area (m^2 s^{-2}), C_D is the vegetation drag coefficient, φ is the solid volume fraction occupied by vegetation, and A is the vegetation projected area per bed area (m^2 m^{-2}), calculated by vertically integrating the vegetation projected area density a (m^2 m^{-3}) for water column with depth h (m). Here, C_D values around 1 have been obtained in flows with Reynolds numbers (*Re*) high enough to ensure turbulent wakes.

The drag model, Eq. (1), with suggested C_D values may offer an accurate evaluation of the mangroves coastal protection function once it is implemented in coastal hydrodynamic models (Cao et al., 2021). However, actual mangrove forests in the field often have more complicated root systems than model mangroves examined in flume experiments; thus, the applicability of the drag model to field mangrove forests needs to be tested. To date, only a few studies have quantified vegetation drag in field mangrove forests. Mullarney et al. (2017) and Horstman et al. (2021) quantified the drag from pressure gradient by measuring water level differences along transects, however, C_D was not derived because the parameter a was not quantified. Only Mazda et al. (1997) obtained field estimates of C_D by putting additional efforts in measuring vegetation morphology for a. The derived C_D showed high variability ranging from 0.4 to more than 10 in tide-driven currents where turbulent wakes are usually expected, which contradicts the results of laboratory-based studies. However, their estimates of C_D were based on velocity measured at a single point while derivation of C_D requires velocity profiling as indicated in Eq. (1). Also, the measurement of vegetation morphology was rather limited in terms of sampling number to obtain the representative (or spatially averaged) value of a in more than 100-m long transects. Thus, the reliability of the derived C_D is questionable, and we concluded that the drag model, Eq. (1), has not been adequately tested in field mangrove forests yet.

The feasibility of the drag model, which is attributed to parameter *a* in Eq. (1), also needs to be established. This parameter is labor-intensive to obtain in the field because it is significantly influenced by tree density and individual tree morphology and could be highly heterogeneous horizontally and vertically. Therefore, implementing the drag model in coastal hydrodynamic models is challenging, especially in a forest-scale simulation (but see Horstman et al., 2015 and Willemsen et al., 2016). In fact, numerical modeling studies often parameterize mangrove drag effects in the bed roughness parameter without accounting for the spatial heterogeneity of vegetation morphological structures (Li et al., 2012, 2014; Zhang et al., 2012; Menéndez et al., 2019); this may result in an inaccurate representation of the coastal protection function.

Here, we have set two specific objectives in this study. First, we aim to quantify the drag and test the applicability of the drag model, Eq. (1), in a *Rhizophora* mangrove forest in the field. Second, we propose a method to predict the parameter *a* in Eq. (1) to reasonably predict the drag in mangrove forests. Such results would provide insights into implementing the drag model in hydrodynamic models, thus, advancing our understanding of the mangroves coastal protection function. A field survey was conducted in a planted *Rhizophora* mangrove forest. A comprehensive data set on hydrodynamics and vegetation morphology needed for testing the drag model were collected for the first time to fill the knowledge gap between the model- and the field-mangrove forests. The spatially uniform distribution of trees with the same age is characteristic of the relatively homogeneous vegetation morphological structures in the selected forest. The transect established for the drag quantification was 30-m long; this is shorter than in previous studies (Mazda et al., 1997; Mullarney et al., 2017; Horstman et al., 2021). The homogeneous vegetation morphology and the short transect allowed us to estimate *a* with high reliability from a relatively small number of morphological measurements. The short transect also enabled us to confirm the unidirectional flow between the ends of the transect during the tidal cycles. To accurately measure the small water level differences within the 30-m long distance which cannot be achieved by usual pressure sensors, we applied a water leveling method as described in this study. For the second objective, we applied a predictive model of *Rhizophora* root morphological structures developed in Yoshikai et al. (2021a) for the parameter *a*, and examined the predictability of drag in the forest using the drag model Eq. (1) using the predicted values of *a*.

2. Materials and Methods

2.1 Study site overview and transect setting

This study was conducted in a planted mangrove forest (locally known as Bakhawan Ecopark) found at the mouth of Aklan River in the province of Aklan, Panay Island, Philippines (Fig. 1a, b). The plantation of *Rhizophora apiculata* started in a mudflat in the early 1990s (Duncan et al., 2016). Subsequent plantations were conducted periodically, producing zones characterized by *R. apiculata* stands with different ages (e.g., ~10 years old, ~20 years old, and ~30 years old). The tide is semi-diurnal with the highest amplitude of 2.0 m. Except areas facing the Aklan River mouth, the flows in the forest and creeks are basically tide-driven. The forests and creeks are sheltered from waves by a sandbar (Fig. 1b).

A reconnaissance of the mangrove areas was conducted and 17-year-old (as of 2018) *R. apiculata* stands were chosen as the drag measurement site (Fig. 1c, d). The site is characterized by well-developed above-ground root systems, uniformly sized and evenly distributed trees, and relatively energetic flows. Here, trees were planted following a 1.5 m × 1.5 m spacing rule. The canopy is closed and sheltered from winds. This is also the site where the morphological structures of above-ground roots were investigated in Yoshikai et al. (2021a) (referred to as site Bak1).

The transect for drag measurement was established on September 9, 2018, a day before the drag measurement was carried out. A reference tree was first identified and located at the center of the transect (Fig. 1c). A visual confirmation was then made such that the above-ground root structures of the reference tree do not deviate largely from those of the surrounding trees in terms of complexity. A 30-m long transect along the major flow direction (A–B; Fig. 1c), which was determined visually, was set during the ebb tide. Afterwards, the x-coordinate was defined to align with the direction of mean flow during ebb tide (the major axis is shown in Fig. 2d), the y-coordinate oriented laterally, and the z-coordinate oriented vertically with z = 0 m at the bed. The x-coordinates of A and B were defined as x_1 and x_2, respectively.

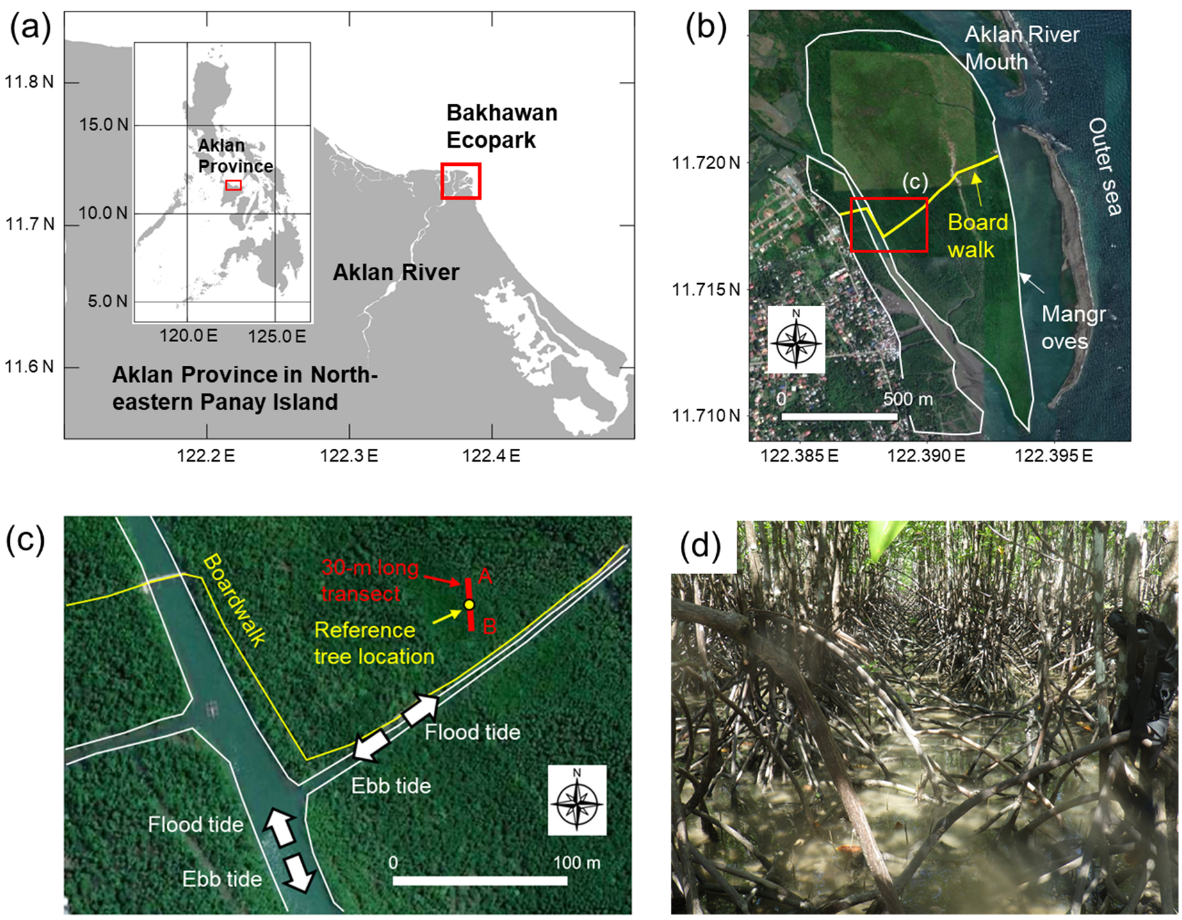

Figure 1. Location of the study site – (a) Bakhawan Ecopark in Aklan province, Panay Island, Philippines; satellite images (Google Earth) of (b) the overview of Bakhawan Ecopark, (c) locations of transect A–B and the reference tree for drag measurement; and (d) photo of the drag measurement site taken near the reference tree. Shoreline data are from the Global Self-consistent, Hierarchical, High-resolution Shorelines (GSHHG) database.

2.2 Measurement of vegetation variables

To obtain the value of the spatially averaged vegetation projected area density, a (m^2 m^{-3}), the morphological structures of above-ground roots and stems around the reference tree were extensively measured from September 13–18, 2018. Data on some trees, including the reference tree, are shown in Yoshikai et al. (2021a). Ten additional trees were compiled and added for a total of 23 trees for this study. The information on the locations of the measured trees are provided in Fig. 2a. Some information on the vegetation parameters is provided in Table 1. Here, the *R. apiculata* trees have multiple stems, where one tree has 3–7 stems. When the main stem of a tree could not be identified in the field, the diameter of the largest stem was used as DBH (diameter at breast height) of the tree.

Table 1. Vegetation and topography information in the study site.

Parameter	Unit	Value
Forest age	years	17
Tree density (n_{tree})	trees m^{-2}	0.36
Number of measured trees (N_{tree})	trees	23
Mean and standard deviation of DBH	m	0.066 ± 0.013
DBH range of measured trees	m	0.045–0.105
DBH of the reference tree	m	0.076
Mean root diameter	m	0.03
Scaling parameter (α in Eq. (9))	m^{-1}	$10^{-3.59}$
Scaling parameter (α_1 in Eq. (9))	–	-2.04
Scaling parameter (β in Eq. (9))	m	0.08
Scaling parameter (β_1 in Eq. (9))	–	15.38
Root angle of approximated root shape (θ in Eq. (11))	degree	-34.5
Ground level at A relative to near the reference tree	m	0.045

Ground level at B relative to near the reference tree	m	-0.049

As described in Yoshikai et al. (2021a, b), four parameters of root were measured; these are height (HR, m), horizontal distance (L, m), angle (θ, degree), and diameter (D_{root}, m). Then, following Ohira et al. (2013), the shape of each root projected from the mean flow direction was estimated from quadratic curve approximation as

$$z = -\frac{HR + L\tan\theta}{L^2}\left(\frac{y}{\cos\psi}\right)^2 + (\tan\theta)\left(\frac{y}{\cos\psi}\right) + HR \quad (2)$$

where ψ is the azimuth angle of root to the mean flow direction; here, $y = 0$ at the location where a root emerges, i.e., the position of y-axis varies for each root. Because the azimuth root angles were not measured, a random number for ψ was given for each root in the range $0° \leq \psi < 90°$ using the random number generator in MATLAB. The projected area of one root can be estimated by multiplying D_{root} with the root length provided by Eq. (2). Similarly, root volume can be estimated from these parameters. By summing the projected areas of all roots in a tree per vertical height, dz (m), the whole-tree root projected area per dz, $a_{root,i}(z)$ (m tree^{-1}, here and hereafter; i denotes tree index), is obtained; a value 0.01 m was used for dz throughout this manuscript.

The stem diameter at 1.3 m height was also measured for the 23 trees. When the root in a tree exceeds the 1.3 m height, the diameters above the highest root were measured. Some stems branched from other stems, and in such cases, the height of the branching point was also measured. Then, the whole-tree stem projected area per dz, $a_{stem,i}(z)$ (m tree^{-1}), was estimated by approximating it as a patch of vertical cylinders whose stem density varies with height depending on the branching of the stems.

Three-dimensional point clouds of the measurement site were obtained using a hand-held GeoSLAM Horizon laser scanner (GeoSLAM Ltd., Nottingham, UK) for the purpose of site visualization (Fig. 2a). From the point clouds, locations of trees were identified, and tree density of the site, n_{tree} (tree m^{-2}), was computed from the visualized tree locations (Table 1).

From the derived parameters $a_{root,i}$, $a_{stem,i}$, and n_{tree}, the vertical profile of the parameter a was calculated as

$$a(z) = \frac{n_{tree}\sum_{i=1}^{N_{tree}}\left(a_{root,i}(z)+a_{stem,i}(z)\right)}{N_{tree}} \tag{3}$$

where N_{tree} is the number of measured trees (Table 1). Here, due to the randomness in the azimuth angle in Eq. (2), the estimated value of a has some uncertainties. In this regard, the value of a was computed repeatedly for 20 times, and the median value was taken as the representative value of a in the area.

2.3 Measurement of hydrodynamic variables

The measurement of hydrodynamic variables for drag quantification was conducted on September 10 and 11, 2018, which were spring tide conditions. A pressure sensor (U20L-04, Onset Computer Corporation, USA), four electromagnetic velocity meters (EM; Infinity-EM, JFE Advantech, Japan), and one Acoustic Doppler Velocimeter (ADV; Nortek Vector, Norway) were deployed around the reference tree (Fig. 2a) for the two-days measurement. The EMs were deployed to measure the near-bed velocities behind (P1), in front (P3), and the sides (P2, P4) of the reference tree relative to the flow direction during the ebb tide (Fig. 2a, b). The body of EM was buried in the mud to position the probe at 5 cm above the bed as done in Schettini et al. (2020). The ADV was deployed around 3 m away from the reference tree in a downward-looking orientation (Fig. 2a, c), where the center of the sampling volume was placed at 5 cm above the bed for bed drag quantification (Pope et al., 2006). The ADV was set to collect data with 16 Hz for 1 minute (960 samples) every 10 minutes. The pressure sensor and

EMs were also set to collect data every 10 minutes. Using data from the deployed EMs, it was confirmed that the flows had a distinct axis and did not rotate during the tidal cycles (Fig. 2d).

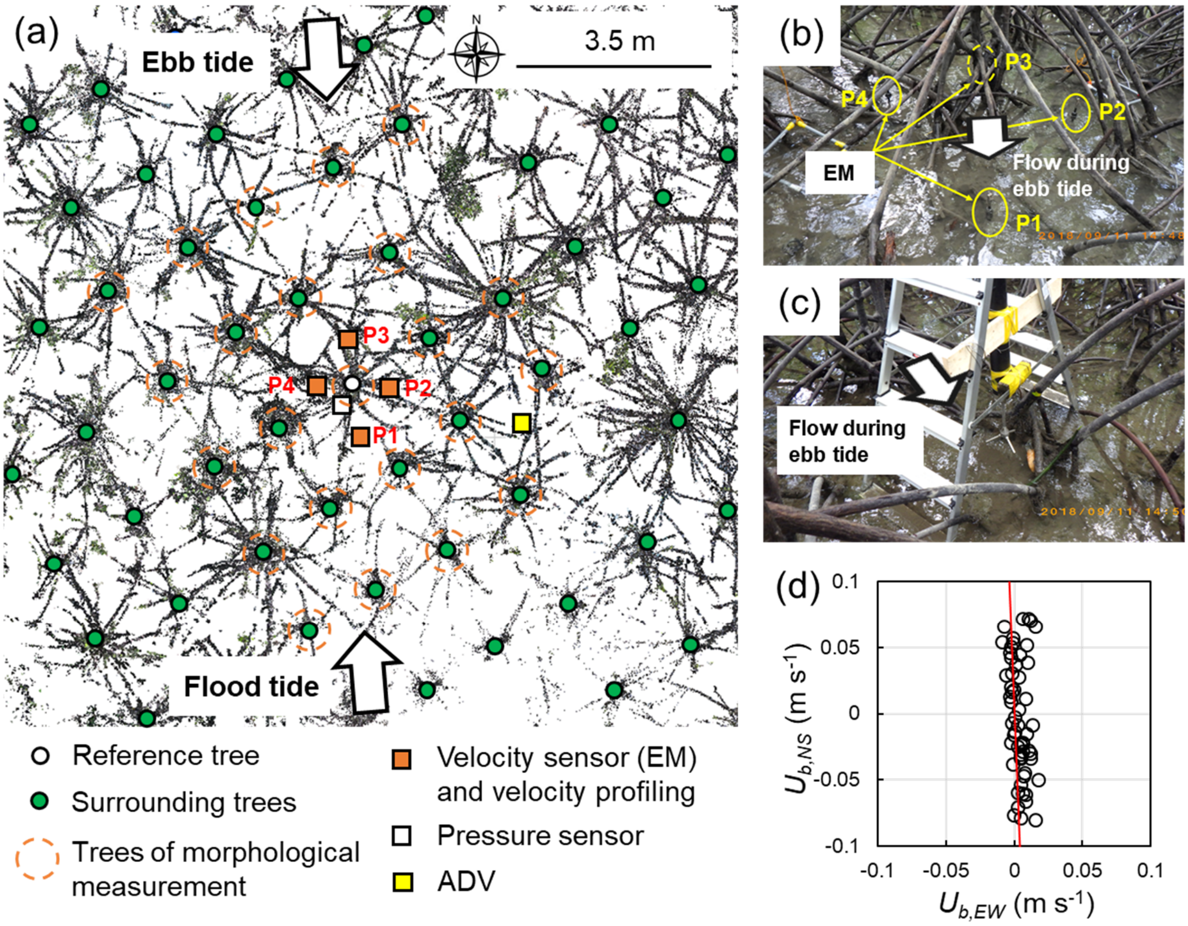

Figure 2. Visualization of the drag measurement set-up: (a) top view of point clouds around the reference tree with information on the locations of measured trees and deployed sensors (The point clouds shown were cropped at heights between 0.1–1.7 m for a better visualization of the root systems); photos of (b) velocity sensors (EM) deployed near the bed around the reference tree (P1–P4) and (c) deployed ADV; and (d) near-bed horizontal flow velocities of the eastern ($U_{b,EW}$) and northern ($U_{b,NS}$) components indicating the major axis (red line) during the measurement period (September 10–11, 2018) obtained by averaging the velocities from the four EMs.

The water level differences between the transect ends A and B, $\Delta\eta$ (m), were measured during the ebb tides using the water leveling method. A schematic of the measurement setup is shown in Fig. 3a. The method is based on the principle that the water level at both ends of a conduit will equalize based on atmospheric pressure. Plastic poles were installed at the transect ends A and B and a 35-m long plastic tube (inner and outer diameters: 6 and 8 mm, respectively) spanned between the poles as illustrated in Fig. 3a. Also, a 1.5-m long plastic tube with the same inner and outer diameters was placed onto pole B vertically (Fig. 3a, b). When the ground was submerged during flood tide on a measurement day, the water connectivity within the tubes was ascertained by removing any trapped air from the upward-oriented tube end using a syringe. This made the water level inside the tube equalized at a location where the downward-oriented tube end is placed, hence the water levels at A ($\eta(x_1)$) and B ($\eta(x_2)$) were made visible at B (Fig. 3c). The downward orientation of the tube end was to prevent the effects of pressure created by flows on the water level inside the tube. When the water became still during high tides, the same level of $\eta(x_1)$ and $\eta(x_2)$ was confirmed. During ebb tides, $\Delta\eta$ was measured using a caliper with 0.1 mm resolution every 10 minutes synchronized to the timing of data collection by the deployed sensors (Fig. 3c). The $\Delta\eta$ was recorded as 0 mm when the water level difference was too small to measure even though the waters were flowing.

The water depths at A, B, and near the reference tree were measured manually when the water was still at high tide. From these water depths, the ground levels at A and B relative to the site near the reference tree were calculated (Table 1).

In conjunction with the sensor data collection and the water level difference measurement, vertical profiling of flow velocity was conducted at the four locations around the reference tree (P1–P4; Fig. 2). An electro-magnetic current meter equipped with a pressure sensor (AEM213-DA, JFE Advantech) was used for the profiling. The sensor is connected to a display unit with a cable and collects data at 1 Hz; one person stood on the root system of the reference tree above the water surface and slowly moved the sensor down (~1.0 cm s^{-1}) from the water surface to the bottom using a cable. When the water became shallower than around 20 cm, a propeller velocimeter (CR-11, Cosmo Riken, Japan) was used for the profiling instead of the AEM213-DA. Its small propeller (~ 2 cm diameter) made it possible to measure velocity within a thin layer and is well-suited to profile shallow waters. In this case, the flow velocities along the transect (x-axis) at the surface, middle, and bottom layers were measured at the four locations around the reference tree.

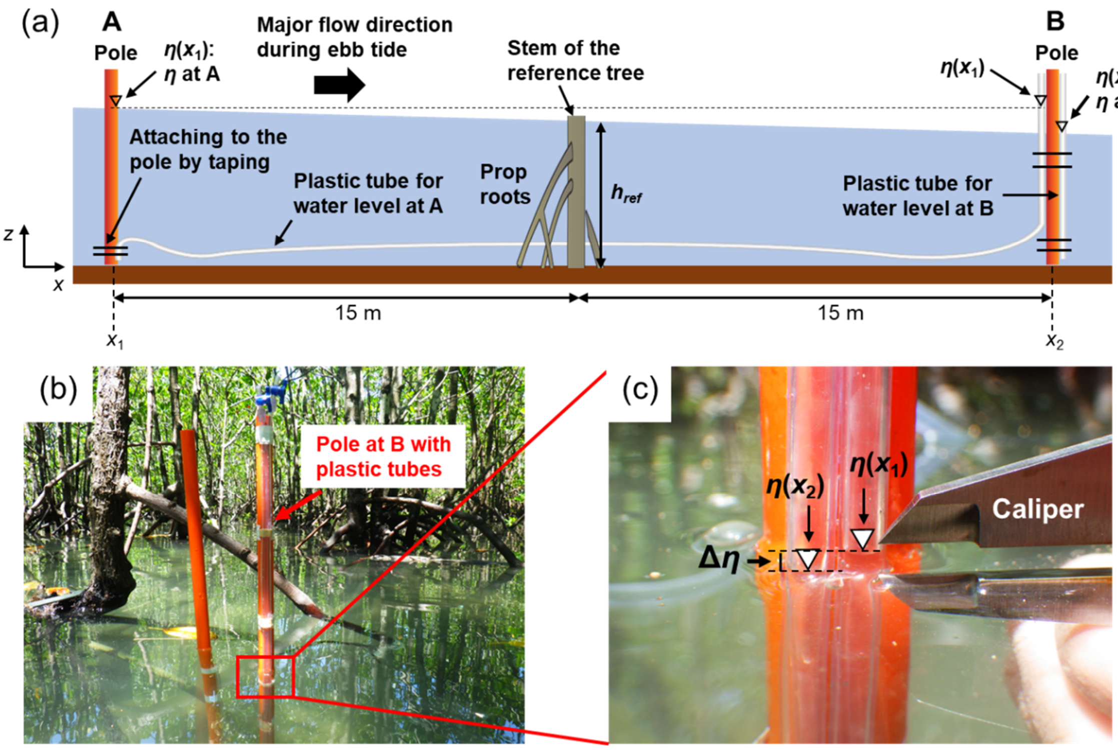

Figure 3. Water level difference measurement: (a) schematic diagram of setup; photos of (b) the pole set at B; and (c) a close view of the plastic tubes attached to the pole showing the water level difference ($\Delta\eta$) between A and B. The η is the water level (m), and h_{ref} is the water depth near the reference tree (m). Note that the schematics is not drawn to scale and the ground level slope is not depicted in the diagram.

2.4 Data processing and bed drag estimation

To obtain the streamwise mean flow velocity profile, the velocities along the x-axis, which were measured by the AEM213-DA, were binned using 0.05-m depth-width and averaged in each bin. The channel mean velocity, U, was calculated by averaging the mean velocities in the bins (or layers, in the case of data from the propeller velocimeter) of the four locations (P1–P4), based on the assumption that the average of the four locations represents the spatial average in the area. To check the validity of this assumption, a particle tracking velocimetry (PTV) survey was conducted around the reference tree in March 2019. See Text S1 and Fig. S1 for the details.

The bed drag, F_{bed} (m^2 s^{-2}), was quantified from the measured Reynolds stress provided by the ADV data (see Text S2 for the details). A bed drag coefficient (C_{bed}) was then determined by fitting the measured F_{bed} and U in following equation of the quadratic drag law (Biron et al., 2004)

$$F_{bed} = C_{bed} U|U| \tag{4}$$

where the value of C_{bed} was determined as 4.2×10^{-3} with $R^2 = 0.55$ (see Fig. Text S2 and Fig. S2). This equation was used to compute the bed drag in the subsequent analyses.

2.5 Estimation of vegetation drag and drag coefficient

Drag by vegetation was quantified from the depth-averaged momentum balance. The inertial terms were significantly small compared to the pressure gradient (more than 20 times smaller), and thus they were neglected as done in other works (Nepf, 1999; Mullarney et al., 2017; Monismith et al., 2019; Horstman et al., 2021). The momentum balance can be then reduced to

$$g\frac{d\eta}{dx} = -\frac{F_{veg,obs}}{h} - \frac{F_{bed}}{h} \tag{5}$$

where g is the gravitational acceleration (m s^{-2}), h is the water depth (m), and $F_{veg,obs}$ is the vegetation drag (m^2 s^{-2}) quantified from field data. Here, we assumed that the water flux is conserved between the transect, $U(x, t)h(x, t) = U_{ref}(\mathrm{t})h_{ref}(\mathrm{t})$, where U_{ref} and h_{ref} are channel mean velocity and water depth near the reference tree, respectively, and the bed slopes between A–reference tree and B–reference tree are constant. Then, following Lentz et al. (2017), Eq. (5) can be rearranged by horizontally integrating between x_1 and x_2 as

$$\langle F_{veg,obs}\rangle(x_2 - x_1) = -g\Delta\eta \int_{x_1}^{x_2} h\,dx - \langle F_{bed}\rangle(x_2 - x_1) \quad (6)$$

where the angle bracket denotes the spatial average between the transect ends A–B and $\langle F_{bed}\rangle(x_2 - x_1) = C_{bed} \int_{x_1}^{x_2} U|U|\,dx$. This equation gives estimates of the mean vegetation drag between the transect, $\langle F_{veg,obs}\rangle$. Similarly, by assuming that value of C_D does not vary between the ends of the transect, integration of the drag model Eq. (1) between x_1 and x_2 yields

$$\langle F_{veg,model}\rangle(x_2 - x_1) = \frac{1}{2} C_D \int_{x_1}^{x_2} \frac{AU|U|}{1-\varphi}\,dx \quad (7)$$

The value of C_D was derived by equating Eqs. (6) and (7) for each measurement.

2.6 Prediction of drag using a *Rhizophora* root model

The *Rhizophora* root model developed in Yoshikai et al. (2021a) was applied as a predictor of a in the drag model, Eq. (1). This model basically predicts the vertical distribution of root density per tree and has successfully predicted the complex root morphological structures in various *Rhizophora* mangrove forests (Yoshikai et al., 2021a). The model assumes that the following equation applies for any root in root system of a tree

$$HR_k = HR_{max} S^{(k-1)} \quad (8)$$

where HR_k and HR_{max} are the root heights (m) of k^{th} highest and the highest root in a root system, respectively, and S is a scaling factor. The parameters S and HR_{max} can be expressed as functions of DBH, and thus, HR_k is a function of DBH as

$$HR_k = (\beta_1 \text{DBH} + \beta)(1 - \alpha \text{DBH}^{\alpha_1})^{(k-1)} \quad (9)$$

where β, β_1 and α, α_1 are the scaling parameters for HR_{max} and S, respectively. The values of these parameters for our study site were derived in Yoshikai et al. (2021a) (Table 1). Similarly, if the t^{th} highest root is the one with the minimum height in a root system, t is the largest integer number that satisfies

$$HR_t = (\beta_1 \mathrm{DBH} + \beta)(1 - \alpha \mathrm{DBH}^{\alpha_1})^{(t-1)} \geq HR_{min} \tag{10}$$

where HR_{min} is the critical height (m) to be given as a model parameter. From Eqs. (9), (10), the vertical variation of root density per dz in a tree is modeled.

To compute the root projected area from the modeled root density, an empirical relationship of $n_{root,i}(z)$ and $a_{root0,i}(z)$ provided in Fig. S3 was used, where $n_{root,i}(z)$ is the number of roots per dz in tree i (root m^{-1} tree^{-1}), and $a_{root0,i}(z)$ is the root projected area per dz with zero azimuth angles (m tree^{-1}). The strong linear relationship between $n_{root,i}(z)$ and $a_{root0,i}(z)$ suggests that the individual roots can be approximated to a single linear shape assuming a uniform root diameter as

$$z = (\tan\theta)\left(\frac{y}{\cos\psi}\right) + HR \tag{11}$$

If Eq. (11) is applied, the slope of the $n_{root,i}(z)$ and $a_{root0,i}(z)$ relationship stands for $D_{root}dz/\sin(-\theta)$. By applying the average root diameter (D_{root} = 0.03 m; Table 1), the value of the root angle θ was determined as -34.5° for our study site (Fig. S3a; Table 1). As with the field data, random numbers were given to ψ in Eq. (11) for each root. The parameter a was then calculated from the modeled root projected area using Eq. (3) for 20 times, and the median value was taken as the representative value of model prediction; the observed value was used for $a_{stem,i}(z)$, which can be easily measured in the field.

Different parameter settings of HR_{min} were tested for predicting a by changing the values from 0.01 to 0.1 m with 0.01 m interval. The root angle (θ = -41.9°; Fig. S3b) determined for another mangrove forest (Fukido mangrove forest in Ishigaki Island, Japan; site Fuk in Yoshikai et al., 2021a) was also tested. The modeled a was then used in the drag model Eq. (1) for prediction of the drag exerted in the measurement site.

3. Results

3.1 Vegetation parameters

Figure 4 shows the vertical profile of the parameter a with component-specific projected areas of the 1^{st} order root, higher order root, and stem, where the root order indicates the level of branching from the stem. The variations in a attributed to the random factor of root azimuth angle (Eq. (2)) were negligibly small, less than 2% of the value shown in Fig. 4; thus these variations were not considered in the subsequent results. The slightly lower projected area of stems at the lower portion (z < 0.3 m) is attributed to the branching of stems. The parameter a showed significant vertical variation and the root is clearly the dominant factor affecting the value of a compared to the stem. While 1^{st} order roots showed a moderate increase in their projected area towards the bed, the higher order roots showed a drastic increase below 0.3 m height. Consequently, the value of a exhibited a nearly exponential increase with decreasing height and reached 1.06 m^{-1} near the bed (black solid line in Fig. 4). Specifically, the projected area of roots higher than 1^{st} order was almost twice of the 1^{st} order root near the bed (z < 0.1 m), highlighting the importance of the presence of higher order roots in parameter a. The vertical variations in the vegetation solid volume fraction, φ, was around 0.025 at the highest near the bed (Fig. S4).

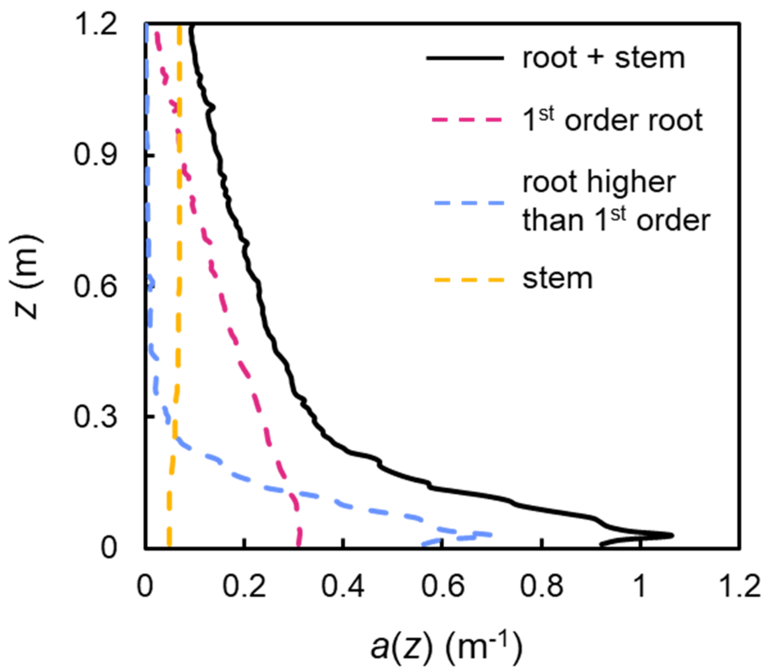

Figure 4. Vertical profile of spatially averaged vegetation projected area density (a, m^{-1}). The values of a were calculated with 0.01 m vertical resolution. The black solid line shows the median values of a from ensemble calculations (N = 20) while the red, blue, and yellow dashed lines show the contributions of 1st order root, higher order root, and stem to a, respectively.

3.2 Measured flow velocity and drag force

Figure 5 shows the time-series of measured hydrodynamic variables on September 10 and 11, 2018. Note that some data on U_{ref} and $\Delta\eta$ are absent due to instrument problems and measurement setup maintenance, therefore the number of measured $\langle F_{veg,obs} \rangle$ is smaller than those of U_{ref} or $\Delta\eta$ (Fig. 5); also, $\langle F_{veg,obs} \rangle$ was not derived when the $\Delta\eta$ recorded was 0 mm. The U_{ref} was generally around 1.5 times larger than the velocities near the bed measured by EM sensors but became comparable when the water depth decreased (h_{ref} < 0.2 m). While these patterns were consistent during the two-days measurement, the U_{ref} on September 10, 14:00, was smaller than the velocity from EM sensors, possibly due to an unreliable measurement of U_{ref} using the propeller velocimeter (Fig. 5b). Velocity magnitude measured by ADV during flood tide was significantly lower than EM-measured velocity or U_{ref} (Fig. 5b, f), probably due to local influence of nearby roots at the upstream side (Fig. 2c).

The variations of the measured $\Delta\eta$ were 1.2–11.4 mm (Fig. 5c, g). The $\Delta\eta$ increased as water depth decreased. Accordingly, the vegetation drag per water volume $\langle F_{veg,obs}\rangle/h_{ref}$ showed an increase with decreasing water depth (Fig. 5d, h). The bed drag per water volume $\langle F_{bed}\rangle/h_{ref}$ was significantly small compared to the vegetation drag $\langle F_{veg,obs}\rangle/h_{ref}$, more than 15 times smaller during most of the measurement time.

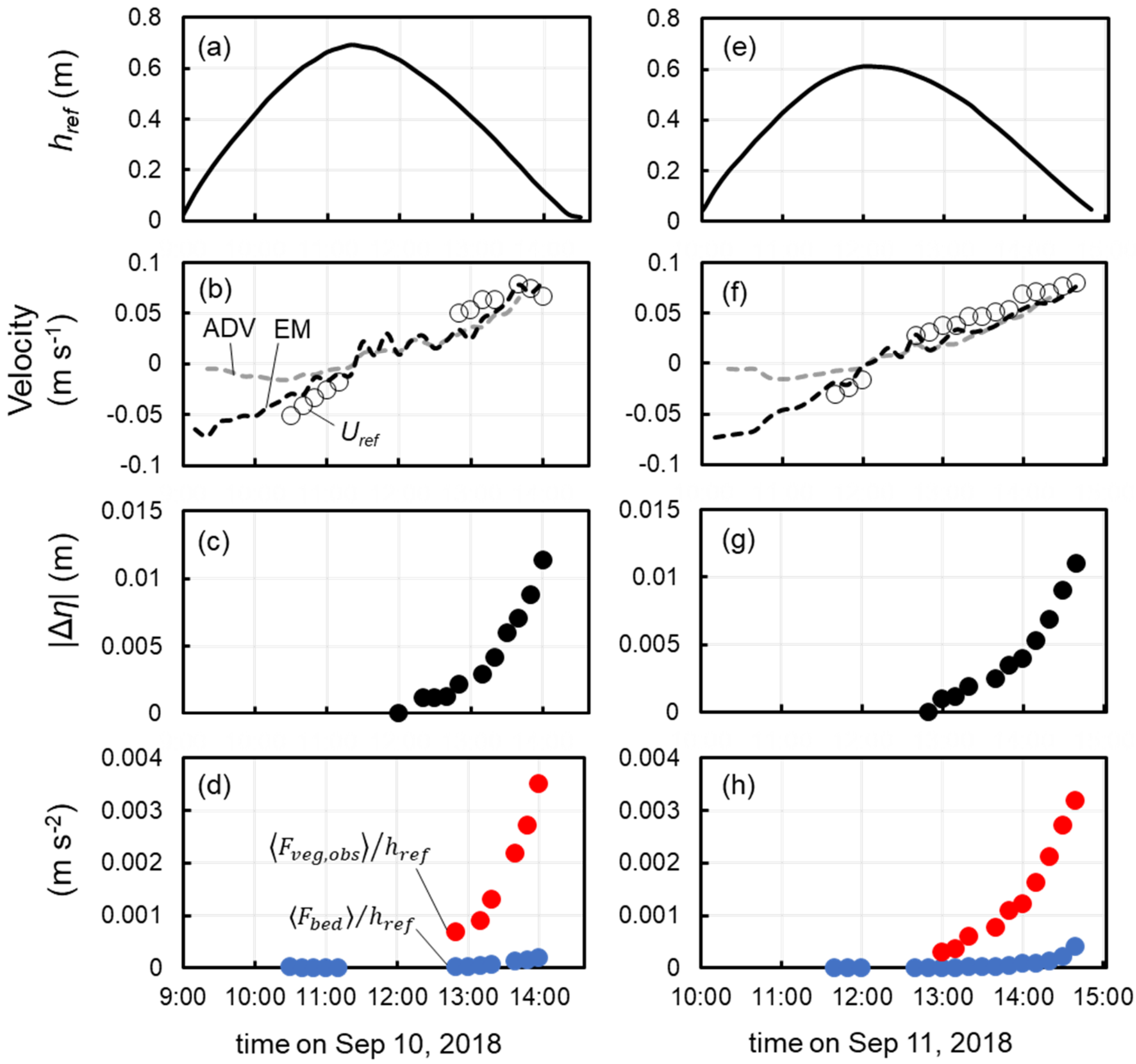

Figure 5. Time-series measurements on September 10 and 11, 2018, respectively, of (a, e) water depth near the reference tree (h_{ref}); (b, f) flow velocity (ADV-measured velocity, average

of EM-measured velocities, and channel mean velocity U_{ref} near the reference tree provided by the velocity profiling); (c, g) water level difference between the ends of transect A–B ($\Delta\eta$); and (d, h) bed $\langle F_{bed} \rangle$ and vegetation $\langle F_{veg,obs} \rangle$ drag divided by h_{ref}. The angle bracket denotes spatial average between A–B. The values for $\langle F_{bed} \rangle$ were given by Eq. (4).

Figure 6 shows the composite of velocity profile normalized by spatially averaged velocity at z = 0.1 m ($u_{0.1}$) for the two-days measurement. The local velocity profiles (u_p) normalized by $u_{0.1}$ showed some variations depending on the measurement locations (P1–4) (Fig. 6a). Overall, the flow velocities measured at the sides of the reference tree (P2, P4) were higher than the front (P3) or back (P1) of the tree at z > 0.25 m. The velocities were greatly attenuated below 0.25-m height and showed smaller variations among the locations. The profile of the spatially averaged velocity (u) also showed significant decrease below 0.25 m (Fig. 6b), corresponding to a significant increase in a (Fig. 4). The profile of u showed agreement with a theoretical predictor of spatially averaged velocity profile (red line in Fig. 6b) derived by Lightbody and Nepf (2006).

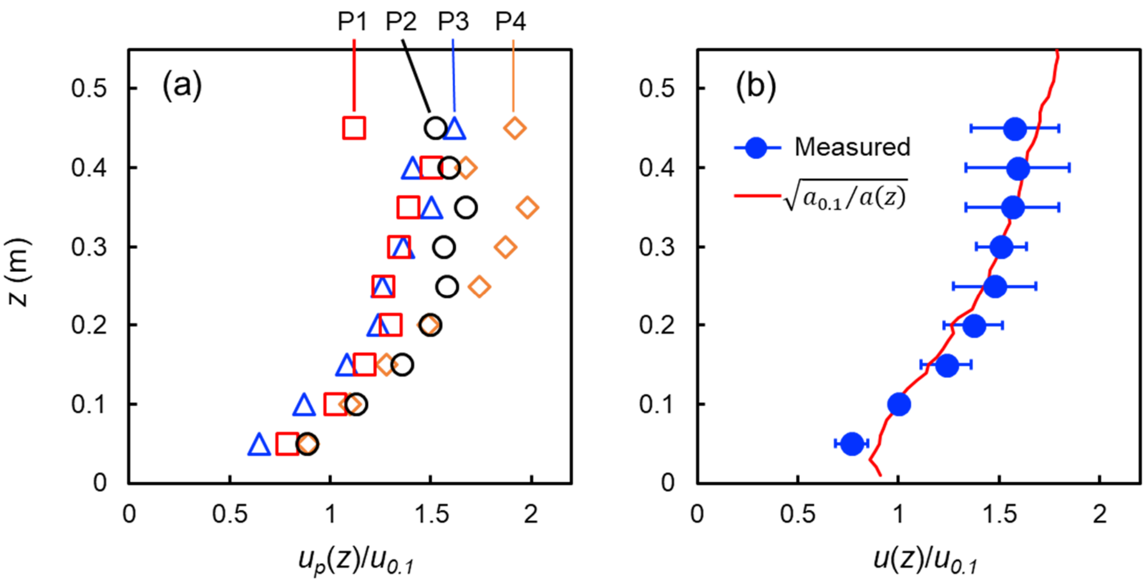

Figure 6. Vertical profile of streamwise horizontal velocity: (a) local velocity measured at P1–P4 (u_p) normalized by the spatial average (P1–P4) of velocity at 0.1 m above the bed ($u_{0.1}$); and

(b) spatial average of velocity (u) normalized by $u_{0.1}$ (markers) with a predictor of $u(z)/u_{0.1}$ (red line), where $a_{0.1}$ is the spatially averaged vegetation projected area density at 0.1 m above the bed. The normalized velocities shown are the mean values of the different velocity measurements during the two-days measurement and the horizontal bars in panel "(b)" indicate the standard deviation.

3.3 Drag coefficient and application of the drag model

The $\langle U^2 \rangle$ and vegetation drag averaged for unit water volume $\langle F_{veg,obs} \rangle / h_{ref}$ showed significant correlation (R^2 = 0.870), but separate line fitting for $h_{ref} > 0.3$ m and $h_{ref} < 0.3$ m exhibited different line slopes (Fig. 7a). Note that the data taken on September 11, 14:00, was excluded from the line fitting as the data of U_{ref} may not be accurate (see Fig. 5b). Instead, the $\langle U^2 \rangle$ and drag averaged for unit vegetation projected area $\langle F_{veg,obs} \rangle / \langle A \rangle$ showed higher correlation (R^2 = 0.901), and separate line fittings did not show significant difference in the line slopes (Fig. 7b).

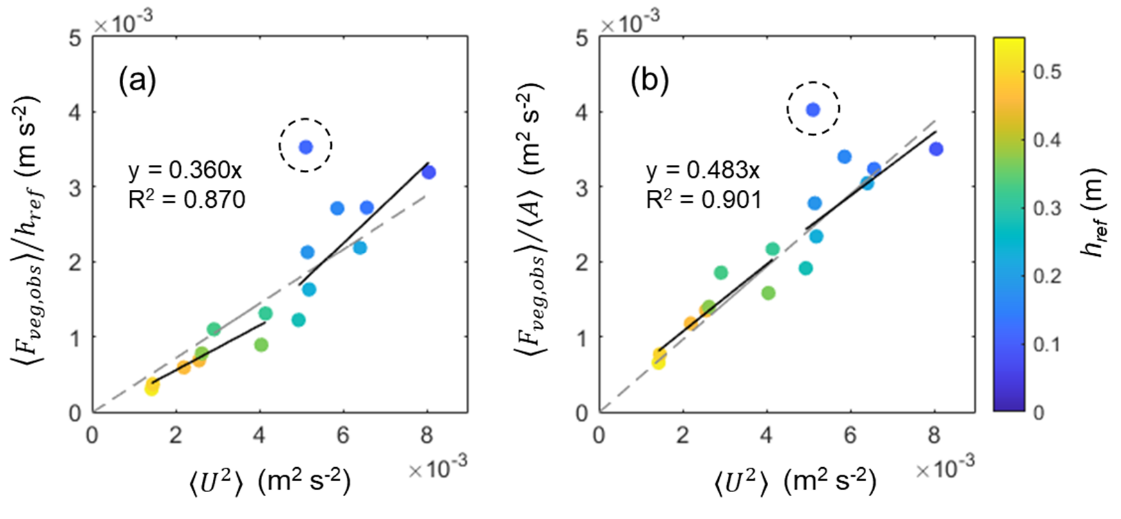

Figure 7. Comparison of the velocity squared with (a) vegetation drag averaged for unit water volume and (b) for unit vegetation projected area. The parameter A is total vegetation projected area per ground area (m^2 m^{-2}) and the bracket denotes spatial average between the ends of transect A–B. The gray dashed line indicates linear fit with intercept fixed at zero while the

black lines indicate linear fit for h_{ref} > 0.3 m and h_{ref} < 0.3 m, respectively; the data enclosed by the dashed circle (data for September 11, 14:40) was excluded from the line fitting.

The value of C_D derived for each measurement using Eqs. (6) and (7) is shown in Fig. 8; a mean value and standard deviation of 1.01 ± 0.18 were obtained. The derived C_D showed close values to the results obtained in laboratory-based studies of Zhang et al. (2015), Maza et al. (2017), and Shan et al. (2019). The Reynolds number, Re, defined using D_{root} as length scale, suggests the fully turbulent structures of root-generated wakes (> 1,000) and the derived C_D showed no dependence on Re. The C_D also did not show dependence on water depth.

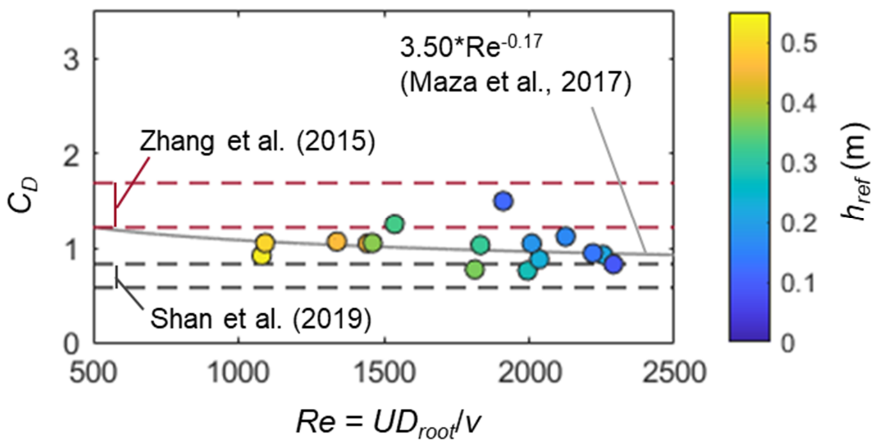

Figure 8. Drag coefficient (C_D) estimated for each hydrodynamic measurement and plotted against the Reynolds number (Re). The Re is defined by root diameter (D_{root}) as length scale and v for kinematic viscosity. The empirical curve obtained by a flume experiment by Maza et al. (2017) and ranges obtained by flume experiments of Zhang et al. (2015) and Shan et al. (2019) are also shown.

Given the independent trend of C_D from Re and water depth and the small variations of the obtained values, it was inferred that C_D can take a constant value in the studied mangrove forest regardless of the timing of tidal cycles. The vegetation drag was then computed as model estimates using Eq. (7), a rearrangement of the drag model Eq. (1), with the mean C_D value

(1.0) and the measured a profile shown in Fig. 4. The result showed a high coefficient of determination (R^2 = 0.86) for the vegetation drag averaged for unit water volume (Fig. 9).

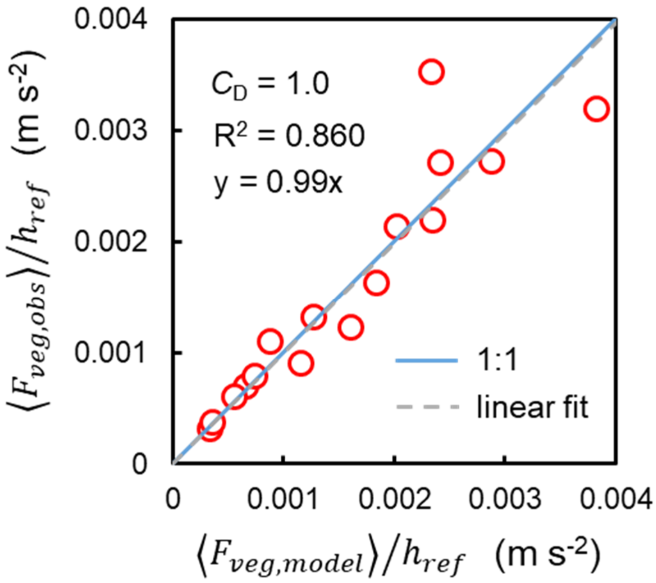

Figure 9. Comparison of measured and modeled vegetation drag. The modeled values were given by Eq. (7), a rearrangement of Eq. (1) with C_D = 1.0, and the measured profile for a shown in Fig. 4.

3.4 Prediction of drag using the *Rhizophora* root model

The *Rhizophora* root model well-predicted the overall vertical profile of a composed of multiple order roots, using a parameter setting of θ = -34.5°, a value determined for the Bakhawan Ecopark study site (Fig. S3a), and HR_{min} = 0.01 m (Fig. 10a). The modeled vegetation drag computed with the modeled a and C_D = 1.0 showed good agreement with the measured drag, with a slope of 1.06 and R^2 = 0.84 of the linear fitted line (Fig. 10b). The use of θ value obtained in another mangrove forest (-41.9°; Fig. S3b) resulted in the underestimation of a due to the steeper angle of the approximated root shape (Eq. (11)) specifically at the lower part (z < 0.3 m) (Fig. 10c). Due to the underestimation of a, the predicted vegetation drag also showed underestimation trend, with the fitted line slope of 1.18, while the R^2 value did not vary significantly compared to when θ = -34.5° (Fig. 10d).

The increase in the value of HR_{min} from 0.01 m to 0.1 m resulted in underestimation of the vegetation drag as seen in the increased slope of fitted line (Fig. 10e). When θ = -34.5°, the increase in slope was almost linear with the increase in HR_{min}; the slope reached 1.17 at HR_{min} = 0.05 m and 1.31 at HR_{min} = 0.10 m. Alternatively, the R^2 value of the line fitting did not change significantly with the changes in HR_{min}. When θ = -41.9°, the slope increased by around 0.12 compared to when θ = -34.5°, and reached 1.46 at HR_{min} = 0.10 m. The R^2 value of the line fitting showed almost same value as the result obtained for θ = -34.5°.

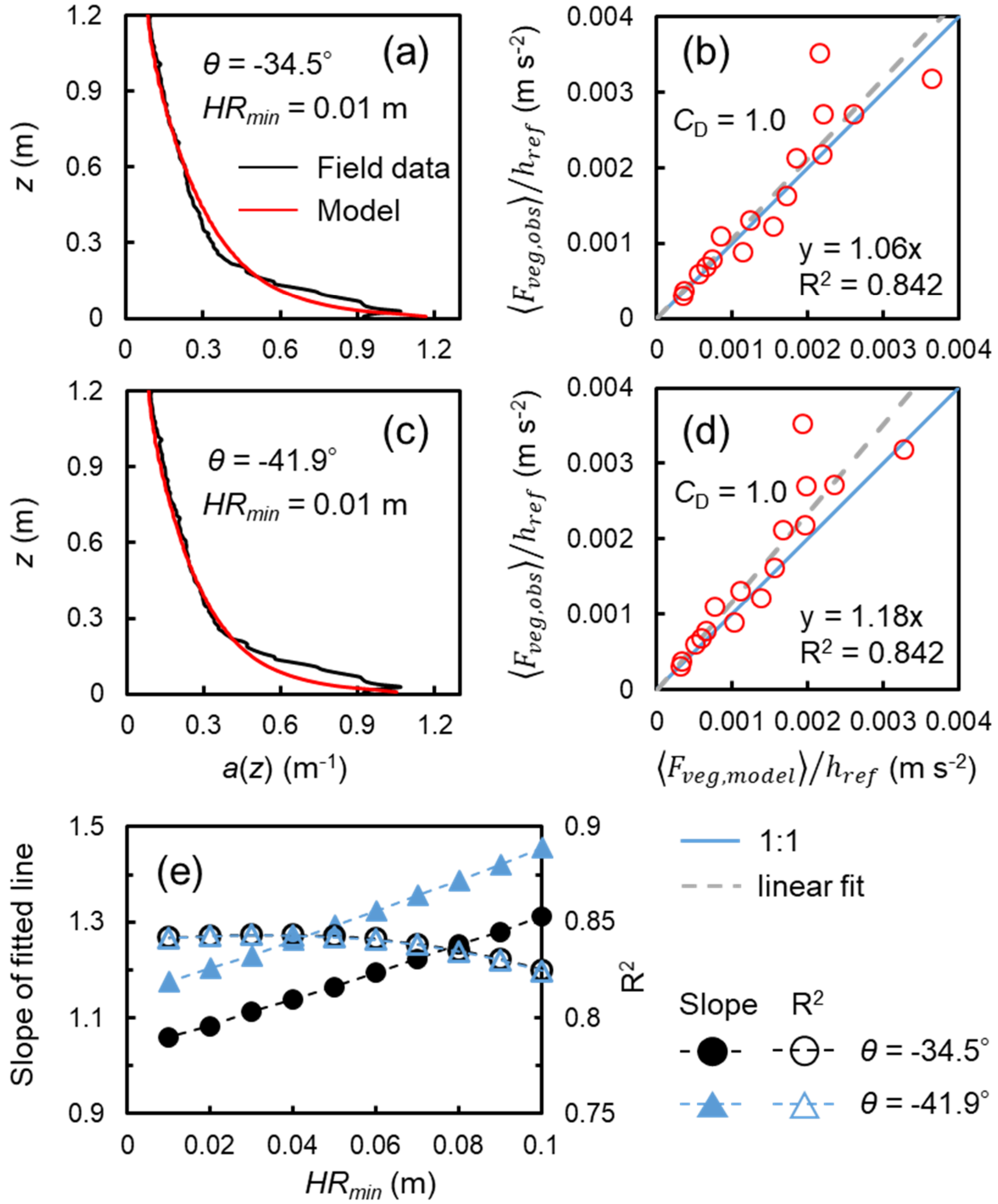

Figure 10. Comparisons of field-measured and modeled (a, c) a and (b, d) vegetation drag using the parameter settings θ = -34.5° and θ = -41.9°, respectively; and (e) changes in the slope and R^2 of the linear fitted line of the relationship between $\langle F_{veg,model} \rangle / h_{ref}$ and $\langle F_{veg,obs} \rangle / h_{ref}$ plotted with the changes in HR_{min} for the two different values of θ. The parameter setting θ = -34.5° is the value derived for the study site (see Fig. S3a) while θ = -41.9° is the value obtained from another mangrove forest (Fukido mangrove forest; Fig. S3b).

4. Discussion

4.1 Flow and drag in the studied field mangrove forest

The spatially uniform distribution of the *Rhizophora* trees with the same age at the site investigated in this study (Bakhawan Ecopark in Aklan, Philippines; Fig. 1d; Fig. 2a) represents a setting that previous laboratory-based studies have examined using model mangroves (Zhang et al., 2015; Maza et al., 2017; in-line distribution configuration in Shan et al., 2019). A notable difference between the field and model mangrove forest is the complexity of the root system. For instance, Maza et al. (2017) used a *Rhizophora* tree model with 24 roots assuming a DBH of 0.2 m, while the reference tree in the study site with DBH of 0.076 m had 96 roots; the latter is way more complicated, and this complexity is not exceptional at all compared with other *Rhizophora* mangrove forests (Yoshikai et al., 2021a, b). Specifically, it was observed that the number of roots higher than 1st order drastically increased below z = 0.3 m, shaping the significant vertical variations in the parameter a. Physical models of such complicated root systems for more realistic representations of the *Rhizophora* root systems in flume experiments could be challenging to make. This emphasizes the importance of the field-based studies for the quantification of drag in a mangrove forest.

The values of a measured in the study site showed comparable values to the results obtained in other mangroves with *Rhizophora* species (Horstman et al., 2015: a = 0.19–1.22 m^{-1} at z = 0.1 m) and mangroves dominated by pneumatophores of *Sonneratia* species (Norris et al., 2017: a = 0.04–1.17 m^{-1}). The value of U measured during the spring tide were 0.08 m s^{-1} at the maximum (Fig. 5b, f), which is also comparable to the velocity measured in other mangrove forests (e.g., Chen et al., 2016; Horstman et al., 2021). The mangrove forest investigated in this study is thus considered to have a typical vegetation projected area density and tidal flow regime that can be observed in other mangrove forests. This implies that the insights obtained in this study are applicable to other mangrove forests.

The normalized local velocity ($u_p/u_{0.1}$) showed larger spatial variations at higher elevation (z > 0.25 m) compared to lower elevation (Fig. 6a). Generally, roots are more clumped around the stem at the higher part of the root system, making locally low root blockage areas especially at the sides of a tree (P2, P4; Fig. 1d). The relatively higher velocity at P2 and P4 may be due to flow redistribution to the low blockage area (Maza et al., 2017), and the lower velocity at P1 or P3 may be due to the influence of wakes generated by roots and stems or velocity deceleration upstream of the clumped roots (Chen et al., 2012). Roots are spread widely at the lower part of the root system (Méndez-Alonzo et al., 2015; Fig. 1d) making a relatively uniform root distribution, which may explain the smaller spatial variations of velocity at lower elevations.

The profile of normalized velocity averaged for P1–P4 (u) showed a good agreement with the theoretical model of Lightbody and Nepf (2006), which predicts the profile of spatially averaged velocity in vegetations with vertically-varying frontal area (Fig. 6b). This model is based on the quadratic drag law of vegetation and assumes a constant C_D throughout the water depth and the examined flow conditions. The model is applicable to a fully developed flow where the viscous and turbulent stresses are significantly smaller than vegetation drag. It has successfully predicted the velocity profile of flow through various types of vegetation (Lightbody and Nepf, 2006; Nepf 2012; Xu and Nepf, 2020). The agreement of u with the model that only uses the profile of a as explanatory variable emphasizes the significant influence of vegetation morphology on flow structures in the studied mangrove forest. This agreement also implies the validity of the assumption that the velocity averaged for P1–P4 represents the spatially averaged velocity.

One key feature observed in the field mangrove forest is the depth dependence of drag per water volume as seen in Fig. 7a. The different slopes of the relationship between $\langle U^2 \rangle$ and $\langle F_{veg,obs} \rangle / h_{ref}$ depending on the water depth indicates the enhancement of drag per water volume relative to flow velocity when the water depth decreased. This may be considered the result of the vertical variation of the parameter a, leading to increased depth-averaged vegetation projected area to exert drag per unit water volume as the water depth decreases (Fig. 4). This highlighted the difference of drag characteristics in *Rhizophora* mangrove forests from an array of vertical emergent cylinders and the difficulty in parameterizing mangrove drag effects in roughness parameters such as Manning's roughness coefficient and Chezy coefficient (Li et al., 2012, 2014; Zhang et al., 2012). Interestingly, the depth dependence observed in the relationship between $\langle U^2 \rangle$ and $\langle F_{veg,obs} \rangle / h_{ref}$ was not evident when the $\langle U^2 \rangle$ was compared with $\langle F_{veg,obs} \rangle / \langle A \rangle$ (Fig. 7b), suggesting that the drag exerted per unit vegetation area solely depends on the square of flow velocity. This signifies that the quadratic drag law is applicable to the studied field mangrove forest.

4.2 Applicability of the drag model in the field mangrove forest

Previous laboratory-based studies for flows in *Rhizophora* mangrove forest showed C_D values around 1 at *Re* high enough to ensure turbulent wakes (Zhang et al., 2015; Maza et al., 2017; Shan et al., 2019). Our field data showed that *Re* estimated using the mean root diameter indicates turbulent wake structures (> 1,000) throughout a tidal phase, and the derived C_D is independent of *Re* (Fig. 8). Interestingly, the C_D derived for the studied field mangrove forest also showed values around 1.0, close to the ones obtained for the model mangroves despite the complicated root systems that field mangroves have. This value also agrees with the value (1.0) which is typically used for the drag coefficient of other type of vegetation (e.g., seagrass) at high *Re* (Nepf, 2012; Kalra et al., 2017; Moki et al., 2020; Cao et al., 2021). The independence of C_D on water depth is consistent with the results of Maza et al. (2017), and Xu and Nepf (2020) who investigated drag exerted by a salt marsh plant *Typha* with vertically varying frontal area.

This study used spatially averaged equations (Eqs. (1), (4)–(7)) for deriving C_D. Therefore, the estimates of C_D could be significantly biased by the error in measuring the channel mean flow velocity, U. While it is challenging to obtain the true value of channel mean velocity and assess the measurement error, we refer to the results of the PTV survey conducted around the reference tree (Text S1, Fig. S1). The results suggest that the velocity averaged for the four locations (P1–P4) deviates 10% to 20% from the PTV-estimated spatially averaged velocity. This deviation leads to C_D error estimates of 20% to 35%, which are close to the variations of the derived C_D values (Fig. 8). We thus consider that the derived C_D in the field mangrove forest may have errors of approximately 20–35% and the variations of the obtained C_D are attributed to the errors in measuring the channel mean flow velocity.

Our observation of the quadratic dependence of drag on velocity (Fig. 7b) and the obtained value of $C_D \approx 1$ (Fig. 8) suggests the applicability of the drag model, Eq. (1), to field mangrove forest settings. The good agreement with the modeled and observed drag shown in Fig. 9 verifies that Eq. (1) is a good model for predicting drag in field mangrove forests. The flow and drag in mangrove forests have been investigated mainly through flume experiments (Zhang et al., 2015; Maza et al., 2017; Shan et al., 2019). Our results imply that the insights obtained by these flume experiments are applicable to field mangrove forests with complicated root structures. Overall, this is the first study that collected sophisticated data set on hydrodynamics and vegetation needed for properly quantifying drag and deriving the drag coefficient and showed the applicability of the drag model proposed by laboratory-based studies to field mangrove forest.

Although our results are consistent with previous laboratory-based studies, the derived drag coefficient showed different trends from Mazda et al. (1997), which obtained large variations in C_D from 0.4 to more than 10. Given the improvement in the experimental design made in this study, we argue that our results more likely represent the actual drag in mangrove forests. On the other hand, it should be noted that compared with our site, the site studied in Mazda et al. (1997) had different vegetation morphological complexities. Specifically, Mazda et al. (1997) reported significantly high vegetation solid volume fraction, $\varphi = 0.15$–0.3, at lower elevation, compared to our study site that showed $\varphi = 0.025$ near the bed (Fig. S4); this is the level where the inertial drag effects or sheltering effects could significantly contribute to or reduce the spatially averaged drag force (Tanino and Nepf, 2008; Liu et al., 2020; Gijón Mancheño et al., 2021), which may not be the case for our study site. Further study is needed to examine the drag model applicability in field mangrove forests with high solid volume fraction. Similarly, there are also some factors that were not investigated in this study. For instance, Shan et al. (2019) demonstrated different drag coefficients between in-line and random tree distributions while the trees are distributed in-line in our study site, suggesting the need for additional investigations in natural mangrove forests. The flow investigated in this study is characteristically fully developed while those in Maza et al. (2017) and Shan et al. (2019) showed different flow and drag characteristics at the leading edge of a mangrove forest. Further field-based studies are needed to consider these aspects.

4.3 Implications for representing mangrove drag effects in hydrodynamic models

Representing mangrove drag effects using Eq. (1) in hydrodynamic models have been challenging because of the need for information on vegetation morphology for the parameter a, which is labor-intensive to obtain in the field. This study presented a measure to predict a in addition to the field estimates of C_D, which none of the previous field-based studies on mangrove drag were able to consider (e.g., Mazda et al., 1997; Horstman et al., 2021). We used the *Rhizophora* root model of Yoshikai et al. (2021a) to predict a, which is based on the allometric scaling of root structures. This model is valid for complicated root systems composed of multiple order roots, and accurately predicted the vertical profile of a in our study site (Fig. 10a). The good agreement of the modeled drag using the field-derived $C_D \approx 1$ and the predicted a with the measured drag (Fig. 10b) suggests that the drag in *Rhizophora* mangrove forests in the field can now be predicted once the input parameters of the *Rhizophora* root model are given. Note that because the roots higher than the 1st order could dominate in a specifically at lower elevations as shown in Fig. 4, the use of Ohira et al. (2013) model, which is valid only for root systems with 1st order roots, may result in large underestimation of a and inaccurate prediction of drag.

The input parameters of the *Rhizophora* root model are basically DBH of individual trees (in Eq. (9)–(10)) and tree density, n_{tree} (in Eq. (3)), in the area to predict drag. These are basic information collected for forest inventories and are easy to measure in the field; these can be even estimated from remotely sensed data such as airborne LiDAR and UAV optical imagery (Fatoyinbo et al., 2018; Zhu et al., 2019). Therefore, we expect that simulating the flows in mangrove forests using hydrodynamic models using implementation of the drag model Eq. (1) is now feasible.

Some considerations should be noted when using the *Rhizophora* root model, especially on its parameter settings. First, the scaling parameters of root systems (Table 1) are site- or species-specific (Yoshikai et al., 2021a, b), thus applying the model to a forest without available information on the scaling relationship requires field survey (see Yoshikai et al., 2021a for the methods in obtaining the scaling relationship in the field). Next, the value of HR_{min} should be properly defined for the site as demonstrated in Fig. 10e. The setting HR_{min} = 0.01 m gave the best estimates of a and drag in our study site; however, this value may not be always applicable to other mangrove forests. For instance, the setting HR_{min} = 0.15 m gave the best prediction of the root morphology of *Rhizophora stylosa* in Fukido mangrove forest (results not shown). Therefore, we suggest the measurement of the minimum root heights in the field to find a representative value of HR_{min} at the site in addition to the parameters for obtaining the scaling relationships. Lastly, the root angle of the approximated linear root shape in Eq. (11) seems to vary depending on the site or species (Fig. S3). The use of root angle determined for Fukido mangrove forest, which is 7.5° steeper than our study site, affected the prediction of the a and the drag to some extent as shown in Fig. 10c–e. The root angle was determined from the relationship between $n_{root,i}(z)$ and $a_{root0,i}(z)$, and both parameters are labor-intensive to obtain in the field. Hence, determining the representative root angle for the site of model application may be challenging. Nevertheless, the responses of the predicted a and drag with the different parameter settings provided in Fig. 10 can be used as benchmark for model uncertainty when applying the settings to other mangrove forests. Notably, the drag can still be predicted with reasonable accuracy using estimates of root angle from the other mangrove forests (Fig. 10c–e), thus highlighting the significance of this work in contributing to a better prediction of drag in mangrove forests.

5. Conclusions

This study presents the drag force and drag coefficient estimated from a 17-year-old planted *Rhizophora* mangrove forest based on comprehensive hydrodynamics and vegetation morphology data collected from the field. The vegetation projected area density, a, showed nearly exponential increase towards the bed mainly due to root branching, highlighting the complex root systems of mangroves. Consequently, the drag averaged for unit water volume showed depth dependence relative to velocity, suggesting the difficulty in parameterizing the drag effects of *Rhizophora* mangroves using bed roughness parameters. Instead, the drag averaged for vegetation projected area depended solely on square of velocity regardless of water depth, thus confirming the adherence of drag in the mangrove forest to the quadratic drag law. The derived drag coefficient, C_D, was comparable with the values derived for model-mangroves in previous laboratory-based studies. Using the mean C_D value, the drag model accurately predicted the measured drag, thus verifying the applicability of the drag model proposed by laboratory-based studies to mangrove forest in the field. We also showed that the *Rhizophora* root model by Yoshikai et al. (2021a) can predict well the value of a – another unknown parameter in the drag model aside from C_D – suggesting the model's usefulness in accurate drag prediction. The input parameters of the *Rhizophora* root model are DBH of individual trees and tree density, which can be easily measured in the field. These results provide a way to use the drag model in hydrodynamic models for representing mangrove drag effects, thus contributing to a better understanding and evaluation of the coastal protection function of mangroves.

Data Availability Statement

Data for this study are available at Zenodo at the following link (https://doi.org/10.5281/zenodo.5760343).

Acknowledgments

This work was supported by Science and Technology Research Partnership for Sustainable Development Program (SATREPS) through the Project "Comprehensive Assessment and Conservation of Blue Carbon Ecosystems and their Services in the Coral Triangle (*Blue*CARES)". We thank Ma. Marivic Pepino, Dr. Wilfredo Campos, Takuya Okamoto, Naoya Kawasaki, Franco Almarza, Rey Rusty Quides, Mohammad Haydrey Aminulla, and Mr. Tsuyoshi Kanda for their support during the field survey, and Dr. Charissa Ferrera for providing language help. We are also grateful to Mr. Allan Quimpo of the Kalibo Save the Mangroves Association (KASMA) and the staff of Bakhawan Ecopark.

References

Biron, P. M., Robson, C., Lapointe, M. F., & Gaskin, S. J. (2004). Comparing different methods of bed shear stress estimates in simple and complex flow fields. Earth Surface Processes and Landforms: The Journal of the British Geomorphological Research Group, 29(11), 1403-1415.

Cao, Z., Zhang, Y., Wolfram, P. J., Brus, S. R., Rowland, J. C., Xu, C., ... & Petersen, M. R. (2021). Effects of different vegetation drag parameterizations on the tidal propagation in coastal marshlands. Journal of Hydrology, 603, 126775.

Chen, Y., Li, Y., Cai, T., Thompson, C., & Li, Y. (2016). A comparison of biohydrodynamic interaction within mangrove and saltmarsh boundaries. Earth Surface Processes and Landforms, 41(13), 1967-1979.

Chen, Z., Ortiz, A., Zong, L., & Nepf, H. (2012). The wake structure behind a porous obstruction and its implications for deposition near a finite patch of emergent vegetation. Water Resources Research, 48(9).

Danielsen, F., Sørensen, M. K., Olwig, M. F., Selvam, V., Parish, F., Burgess, N. D., ... & Suryadiputra, N. (2005). The Asian tsunami: a protective role for coastal vegetation. Science, 310(5748), 643-643.

Duncan, C., Primavera, J. H., Pettorelli, N., Thompson, J. R., Loma, R. J. A., & Koldewey, H. J. (2016). Rehabilitating mangrove ecosystem services: A case study on the relative benefits of abandoned pond reversion from Panay Island, Philippines. Marine pollution bulletin, 109(2), 772-782.

Ezcurra, P., Ezcurra, E., Garcillán, P. P., Costa, M. T., & Aburto-Oropeza, O. (2016). Coastal landforms and accumulation of mangrove peat increase carbon sequestration and storage. Proceedings of the National Academy of Sciences, 113(16), 4404-4409.

Fatoyinbo, T., Feliciano, E. A., Lagomasino, D., Lee, S. K., & Trettin, C. (2018). Estimating mangrove aboveground biomass from airborne LiDAR data: a case study from the Zambezi River delta. Environmental Research Letters, 13(2), 025012.

Friess, D. A., Rogers, K., Lovelock, C. E., Krauss, K. W., Hamilton, S. E., Lee, S. Y., ... & Shi, S. (2019). The state of the world's mangrove forests: past, present, and future. Annual Review of Environment and Resources, 44, 89-115.

Friess, D. A., Yando, E. S., Abuchahla, G. M., Adams, J. B., Cannicci, S., Canty, S. W., ... & Wee, A. K. (2020). Mangroves give cause for conservation optimism, for now. Current Biology, 30(4), R153-R154.

Furukawa, K., Wolanski, E., & Mueller, H. (1997). Currents and sediment transport in mangrove forests. Estuarine, Coastal and Shelf Science, 44(3), 301-310.

Gijón Mancheño, A., Jansen, W., Winterwerp, J.C., & Uijttewaal, W. S. J. (2021). Predictive model of bulk drag coefficient for a nature-based structure exposed to currents. Scientific reports, 11, 3517. https://doi.org/10.1038/s41598-021-83035-0

Gijsman, R., Horstman, E. M., van der Wal, D., Friess, D. A., Swales, A., & Wijnberg, K. M. (2021). Nature-based engineering: a review on reducing coastal flood risk with mangroves. Frontiers in Marine Science, 8, 825.

Giri, C., Ochieng, E., Tieszen, L. L., Zhu, Z., Singh, A., Loveland, T., ... & Duke, N. (2011). Status and distribution of mangrove forests of the world using earth observation satellite data. Global Ecology and Biogeography, 20(1), 154-159.

Heyman, J. (2019). TracTrac: A fast multi-object tracking algorithm for motion estimation. Computers & Geosciences, 128, 11-18.

Horstman, E. M., Bryan, K. R., & Mullarney, J. C. (2021). Drag variations, tidal asymmetry and tidal range changes in a mangrove creek system. Earth Surface Processes and Landforms.

Horstman, E. M., Dohmen-Janssen, C. M., Bouma, T. J., & Hulscher, S. J. (2015). Tidal-scale flow routing and sedimentation in mangrove forests: Combining field data and numerical modelling. Geomorphology, 228, 244-262.

Horstman, E. M., Dohmen-Janssen, C. M., Narra, P. M. F., Van den Berg, N. J. F., Siemerink, M., & Hulscher, S. J. (2014). Wave attenuation in mangroves: A quantitative approach to field observations. Coastal engineering, 94, 47-62.

Kalra, T. S., Aretxabaleta, A., Seshadri, P., Ganju, N. K., & Beudin, A. (2017). Sensitivity analysis of a coupled hydrodynamic-vegetation model using the effectively subsampled quadratures method (ESQM v5. 2). Geoscientific Model Development, 10(12), 4511-4523.

Krauss, K. W., Doyle, T. W., Doyle, T. J., Swarzenski, C. M., From, A. S., Day, R. H., & Conner, W. H. (2009). Water level observations in mangrove swamps during two hurricanes in Florida. Wetlands, 29(1), 142-149.

Lee, X., Massman, W., & Law, B. (2004). Handbook of Micrometeorology: A Guide for Surface Flux Measurement and Analysis. Lee, X., Massman, W., & Law, B. Eds., Atmospheric and Oceanographic Sciences Library, Vol. 29, Kluwer, 250 pp., doi:10.1007/1-4020-2265-4.

Lentz, S. J., Davis, K. A., Churchill, J. H., & DeCarlo, T. M. (2017). Coral reef drag coefficients–water depth dependence. Journal of Physical Oceanography, 47(5), 1061-1075.

Li, L., Wang, X. H., Andutta, F., & Williams, D. (2014). Effects of mangroves and tidal flats on suspended-sediment dynamics: Observational and numerical study of Darwin Harbour, Australia. Journal of Geophysical Research: Oceans, 119(9), 5854-5873.

Li, L., Wang, X. H., Williams, D., Sidhu, H., & Song, D. (2012). Numerical study of the effects of mangrove areas and tidal flats on tides: A case study of Darwin Harbour, Australia. Journal of Geophysical Research: Oceans, 117(C6).

Lightbody, A. F., & Nepf, H. M. (2006). Prediction of velocity profiles and longitudinal dispersion in salt marsh vegetation. Limnology and oceanography, 51(1), 218-228.

Liu, M. Y., Huai, W. X., Yang, Z. H., & Zeng, Y. H. (2020). A genetic programming-based model for drag coefficient of emergent vegetation in open channel flows. Advances in Water Resources, 140, 103582.

Mariotti, G., & Fagherazzi, S. (2012). Channels-tidal flat sediment exchange: The channel spillover mechanism. Journal of Geophysical Research: Oceans, 117(C3).

Maza, M., Adler, K., Ramos, D., Garcia, A. M., & Nepf, H. (2017). Velocity and drag evolution from the leading edge of a model mangrove forest. Journal of Geophysical Research: Oceans, 122(11), 9144-9159.

Maza, M., Lara, J. L., & Losada, I. J. (2019). Experimental analysis of wave attenuation and drag forces in a realistic fringe *Rhizophora* mangrove forest. Advances in Water Resources, 131, 103376.

Maza, M., Lara, J. L., & Losada, I. J. (2021). Predicting the evolution of coastal protection service with mangrove forest age. Coastal Engineering, 168, 103922.

Mazda, Y., Wolanski, E., King, B., Sase, A., Ohtsuka, D., & Magi, M. (1997). Drag force due to vegetation in mangrove swamps. Mangroves and salt marshes, 1(3), 193-199.

Méndez-Alonzo, R., Moctezuma, C., Ordoñez, V. R., Angeles, G., Martínez, A. J., & López-Portillo, J. (2015). Root biomechanics in *Rhizophora mangle*: anatomy, morphology and ecology of mangrove's flying buttresses. Annals of Botany, 115(5), 833-840.

Menéndez, P., Losada, I. J., Beck, M. W., Torres-Ortega, S., Espejo, A., Narayan, S., ... & Lange, G. M. (2018). Valuing the protection services of mangroves at national scale: The Philippines. Ecosystem services, 34, 24-36.

Menéndez, P., Losada, I. J., Torres-Ortega, S., Narayan, S., & Beck, M. W. (2020). The global flood protection benefits of mangroves. Scientific reports, 10(1), 1-11.

Moki, H., Taguchi, K., Nakagawa, Y., Montani, S., & Kuwae, T. (2020). Spatial and seasonal impacts of submerged aquatic vegetation (SAV) drag force on hydrodynamics in shallow waters. Journal of Marine Systems, 209, 103373.

Monismith, S. G., Hirsh, H., Batista, N., Francis, H., Egan, G., & Dunbar, R. B. (2019). Flow and drag in a seagrass bed. Journal of Geophysical Research: Oceans, 124(3), 2153-2163.

Montgomery, J. M., Bryan, K. R., Mullarney, J. C., & Horstman, E. M. (2019). Attenuation of storm surges by coastal mangroves. Geophysical research letters, 46(5), 2680-2689.

Mori, N., Suzuki, T., & Kakuno, S. (2007). Noise of acoustic Doppler velocimeter data in bubbly flows. Journal of engineering mechanics, 133(1), 122-125.

Mullarney, J. C., Henderson, S. M., Reyns, J. A., Norris, B. K., & Bryan, K. R. (2017). Spatially varying drag within a wave-exposed mangrove forest and on the adjacent tidal flat. Continental Shelf Research, 147, 102-113.

Nepf, H. M. (1999). Drag, turbulence, and diffusion in flow through emergent vegetation. Water resources research, 35(2), 479-489.

Nepf, H. M. (2012). Flow and transport in regions with aquatic vegetation. Annual review of fluid mechanics, 44, 123-142.

Norris, B. K., Mullarney, J. C., Bryan, K. R., & Henderson, S. M. (2017). The effect of pneumatophore density on turbulence: a field study in a *Sonneratia*-dominated mangrove forest, Vietnam. Continental Shelf Research, 147, 114-127.

Ohira, W., Honda, K., Nagai, M., & Ratanasuwan, A. (2013). Mangrove stilt root morphology modeling for estimating hydraulic drag in tsunami inundation simulation. Trees, 27(1), 141-148.

Ong, J. E., Gong, W. K., & Wong, C. H. (2004). Allometry and partitioning of the mangrove, *Rhizophora apiculata*. Forest Ecology and Management, 188(1-3), 395-408.

Patalano, A., García, C. M., & Rodríguez, A. (2017). Rectification of Image Velocity Results (RIVeR): A simple and user-friendly toolbox for large scale water surface Particle Image Velocimetry (PIV) and Particle Tracking Velocimetry (PTV). Computers & Geosciences, 109, 323-330.

Pope, N. D., Widdows, J., & Brinsley, M. D. (2006). Estimation of bed shear stress using the turbulent kinetic energy approach—A comparison of annular flume and field data. Continental Shelf Research, 26(8), 959-970.

Primavera, J. H., & Esteban, J. M. A. (2008). A review of mangrove rehabilitation in the Philippines: successes, failures and future prospects. Wetlands Ecology and Management, 16(5), 345-358.

Schettini, C. A., Asp, N. E., Ogston, A. S., Gomes, V. J., McLachlan, R. L., Fernandes, M. E., ... & Gardunho, D. C. (2020). Circulation and fine-sediment dynamics in the Amazon macrotidal mangrove coast. Earth Surface Processes and Landforms, 45(3), 574-589.

Shan, Y., Liu, C., & Nepf, H. (2019). Comparison of drag and velocity in model mangrove forests with random and in-line tree distributions. Journal of Hydrology, 568, 735-746.

Strusińska-Correia, A., Husrin, S., & Oumeraci, H. (2013). Tsunami damping by mangrove forest: a laboratory study using parameterized trees. Natural Hazards and Earth System Sciences, 13(2), 483-503.

Tanino, Y., & Nepf, H. M. (2008). Laboratory investigation of mean drag in a random array of rigid, emergent cylinders. Journal of Hydraulic Engineering, 134(1), 34-41.

Temmerman, S., Meire, P., Bouma, T. J., Herman, P. M., Ysebaert, T., & De Vriend, H. J. (2013). Ecosystem-based coastal defence in the face of global change. Nature, 504(7478), 79-83.

Tomiczek, T., Wargula, A., Lomónaco, P., Goodwin, S., Cox, D., Kennedy, A., & Lynett, P. (2020). Physical model investigation of mid-scale mangrove effects on flow hydrodynamics and pressures and loads in the built environment. Coastal Engineering, 162, 103791.

Tomlinson, P.B., 2016. The Botany of Mangroves. Cambridge University Press, Cambridge.

Willemsen, P. W. J. M., Horstman, E. M., Borsje, B. W., Friess, D. A., & Dohmen-Janssen, C. M. (2016). Sensitivity of the sediment trapping capacity of an estuarine mangrove forest. Geomorphology, 273, 189-201.

Woodruff, J. D., Irish, J. L., & Camargo, S. J. (2013). Coastal flooding by tropical cyclones and sea-level rise. Nature, 504(7478), 44-52.

Xu, Y., & Nepf, H. (2020). Measured and predicted turbulent kinetic energy in flow through emergent vegetation with real plant morphology. Water Resources Research, 56(12), e2020WR027892.

Xu, Y., & Nepf, H. (2021). Suspended sediment concentration profile in a *Typha latifolia* canopy. Water Resources Research, 57(9), e2021WR029902.

Yanagisawa, H., Koshimura, S., Miyagi, T., & Imamura, F. (2010). Tsunami damage reduction performance of a mangrove forest in Banda Aceh, Indonesia inferred from field data and a numerical model. Journal of Geophysical Research: Oceans, 115(C6).

Yoshikai, M., Nakamura, T., Suwa, R., Argamosa, R., Okamoto, T., Rollon, R., ... & Nadaoka, K. (2021a). Scaling relations and substrate conditions controlling the complexity of *Rhizophora* prop root system. Estuarine, Coastal and Shelf Science, 248, 107014.

Yoshikai M, Nakamura T, Suwa R, Rollon R, Nadaoka K (2021b) Measurement and modeling of above-ground root systems as attributes of flow and wave attenuation function of mangroves, in: Mangroves: Ecology, Biodiversity and Management, edited by: Rastogi RP, Phulwaria M, Gupta DK, Springer Singapore, Singapore, pp 279-303.

Zhang, X., Chua, V. P., & Cheong, H. F. (2015). Hydrodynamics in mangrove prop roots and their physical properties. Journal of hydro-environment research, 9(2), 281-294.

Zhang, K., Liu, H., Li, Y., Xu, H., Shen, J., Rhome, J., & Smith III, T. J. (2012). The role of mangroves in attenuating storm surges. Estuarine, Coastal and Shelf Science, 102, 11-23.

Zhu, X., Hou, Y., Weng, Q., & Chen, L. (2019). Integrating UAV optical imagery and LiDAR data for assessing the spatial relationship between mangrove and inundation across a subtropical estuarine wetland. ISPRS Journal of Photogrammetry and Remote Sensing, 149, 146-156.

Journal of Geophysical Research: Oceans

Supporting Information for

Field measurement and prediction of drag in a planted *Rhizophora* mangrove forest

Masaya Yoshikai[1], Takashi Nakamura[1], Dominic M. Bautista[2], Eugene C. Herrera[2], Alvin Baloloy[3], Rempei Suwa[4], Ryan Basina[5], Yasmin H. Primavera-Tirol[5], Ariel C. Blanco[3], Kazuo Nadaoka[1]

[1]School of Environment and Society, Tokyo Institute of Technology, O-okayama 2-12-1 W8-13 Meguro, Tokyo 152-8552, Japan

[2]Institute of Civil Engineering, University of the Philippines, Diliman, Quezon City 1101, Philippines

[3]Department of Geodetic Engineering, College of Engineering, University of the Philippines, Diliman, Quezon City 1101, Philippines

[4]Forestry Division, Japan International Research Center for Agricultural Sciences (JIRCAS), 1-1 Ohwashi, Tsukuba, Ibaraki 305-8686, Japan

[5]College of Fisheries and Marine Sciences, Aklan State University, New Washington, Aklan, Philippines

Contents of this file

Text S1. Particle tracking velocimetry survey

A particle tracking velocimetry (PTV) survey was conducted on March 20, 2019, during spring tide, to examine the flow field around a reference tree (Fig. 1c). Four downward-looking digital video cameras (RICOH WG-5) were attached on the stem of the reference tree and oriented in such a way that the different camera views covered the entire root system. A pressure sensor was deployed near the reference tree to monitor water depth. Floating particles (represented by leaves of *Moringa oleifera Lam*, 1 cm dimension in average) were prepared prior to the survey. The PTV was conducted twice at different water depths during flood tide (22:00 and 22:40 on March 20, 2019; Fig. S1c). Before releasing the particles, a square scale with known dimension was placed on the water surface seen by each camera view; this was used for image rectification and scaling. The particles were then released, and the movement of particles around the reference tree was monitored by the four video cameras with a rate of 30 frames per second. After the particle release, velocity profiling using an electro-magnetic current meter (AEM213-DA sensor) was conducted at four locations (P1–P4), as performed in the drag survey described in the manuscript. However, note that profiling was not done when the water depth was shallow for the profiling (22:40 on March 20, 2019).

The trajectories of particles were analyzed for each video data using the open-source PTV software TracTrac developed by Heyman (2019). The video data with particle trajectories were rectified and projected to real-world coordinates with a homography matrix determined based on the square scale (Patalano et al., 2017). The projected data from each camera were combined to make one mosaic image with trajectories that covers the entire root system of the tree. The image was partitioned into 10 cm × 10 cm grids, and in each grid, particle displacements per 10 frames ($dt \approx 0.33$ second) were extracted for all particles as displacement samples. The mean particle displacement per dt was calculated by averaging all the displacement samples in a grid, and the mean velocity in the grid was derived from the mean displacement (Fig. S1a–b).

The mean velocities in the grids were averaged, and the major axis component of the averaged velocity was represented as the stream-wise spatially averaged velocity at the water surface, $\langle u \rangle$. The mean velocities of regions where velocity profiling was conducted were also extracted (P1–P4; Fig. S1a–b), and the surface stream-wise velocity averaged for the four locations $\langle u_{p1\text{–}4} \rangle$ were likewise derived. The $\langle u_{p1\text{–}4} \rangle$ was also estimated from the surface velocities measured by the AEM213-DA sensor. The $\langle u_{p1\text{–}4} \rangle$ was then compared with $\langle u \rangle$ to examine the validity of the assumption that the average of the velocities at the four locations, $\langle u_{p1\text{–}4} \rangle$, represents the spatial average in the area, $\langle u \rangle$.

The results showed that the $\langle u_{p1\text{–}4} \rangle$ derived from PTV and current meter sensor are comparable with values 6.3 cm s^{-1} and 6.6 cm s^{-1}, respectively (Fig. S1d), which ensures a certain accuracy of the PTV-derived velocity field. The comparison with $\langle u \rangle$ showed 10% to 20% deviation of $\langle u_{p1\text{–}4} \rangle$ from $\langle u \rangle$. The values of deviation were referred to as errors of estimating the spatially averaged velocity from velocities at the four locations.

Text S2. Acoustic Doppler Velocimeter (ADV) data processing

The velocity data collected by the ADV were despiked using the phase-space method described in Mori et al. (2007). The despiked velocities (eastward, northward, and vertical) were rotated to give the velocities along the *x*, *y*, and *z*-axes, where the instrument tilt was corrected to make the averaged vertical velocity zero (Lee et al., 2004). Bed drag (F_{bed}, m^2 s^{-2}) was then determined from Reynolds stress, ($-\overline{u'w'}$), where u' and w' are the velocity fluctuations of *x*- and *z*-axis components (m s^{-1}), respectively, and the overbar denotes the time average (note that velocities in the equations in the manuscript denote time-averaged values without the overbars).

As shown in Figs. 5b and 5f, the velocity measured by ADV during the flood tides largely deviated from the EM-measured velocity and U, possibly due to the local influence of nearby roots. Thus, the Reynolds stress measured during flood tides might have been affected by the wakes generated by the roots aside from the bottom friction. In this regard, we excluded the data during flood tides when estimating the bed drag coefficient.

The estimated drag coefficient, C_{bed}, was 4.2 × 10^{-3} (Fig. S2). This value is higher but in the same order of magnitude as the drag coefficient observed in muddy tidal environment (e.g., 2.5 × 10^{-3} in Mariotti and Fagherazzi, 2012).

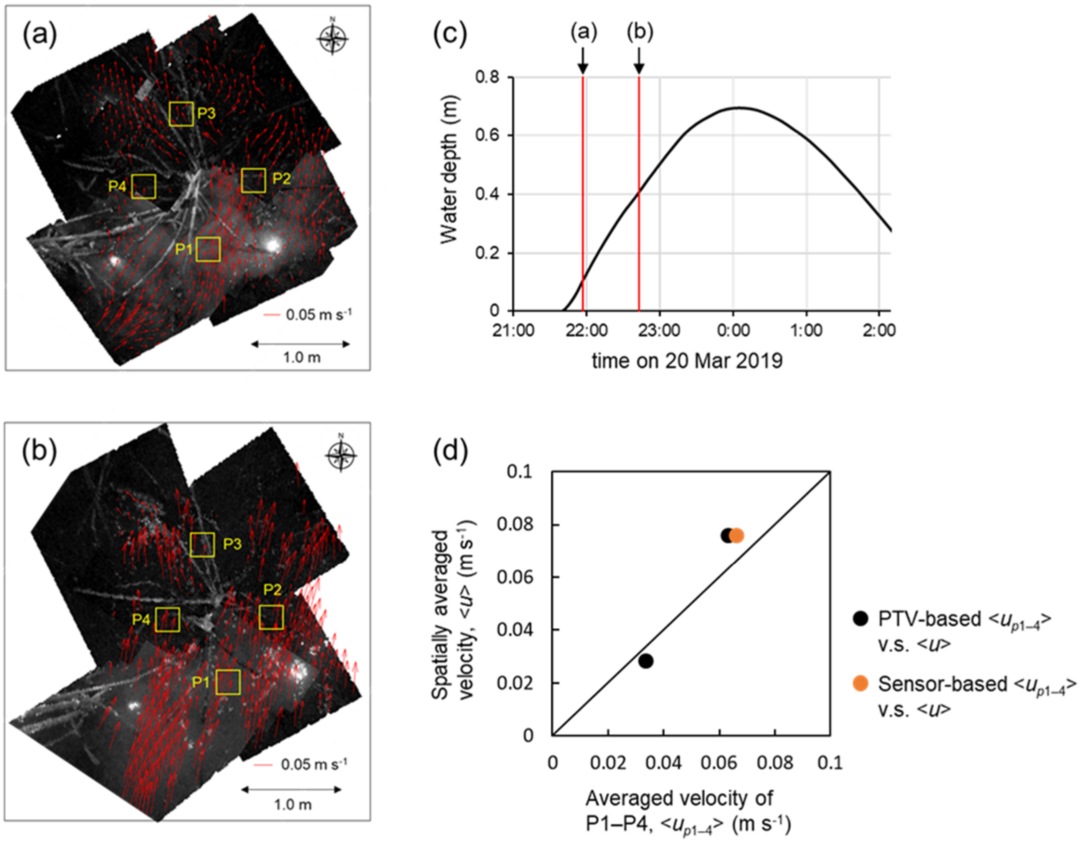

Figure S1. Mean velocity fields around the reference tree at (a) 22:00 and (b) 22:40 on March 20, 2019; (c) time-series data of water depth near the reference tree (the timing when the particles were released are indicated by the red lines); and (d) comparison between $\langle u_{p1\text{–}4} \rangle$ and $\langle u \rangle$.

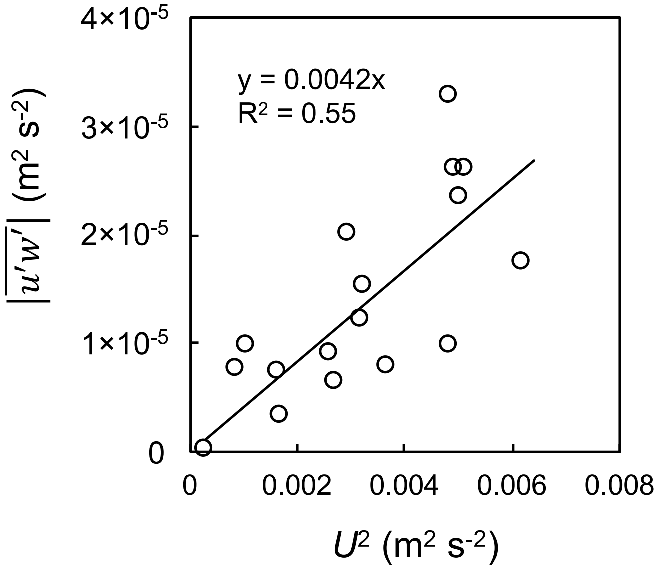

Figure S2. Relationship between U^2 and Reynolds stress $|\overline{\boldsymbol{u'w'}}|$. The slope of the fitted line represents the bed drag coefficient.

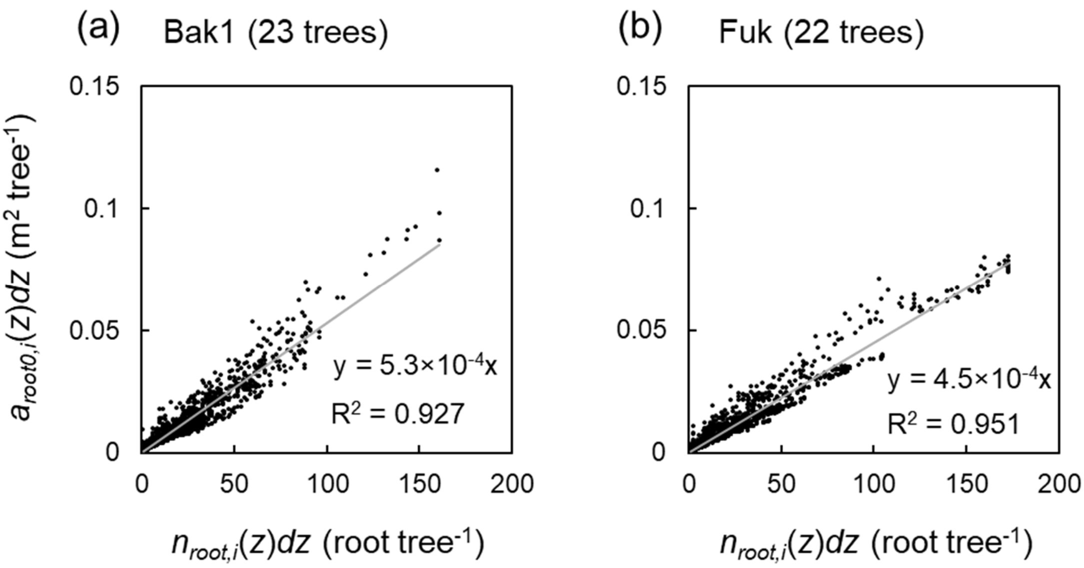

Figure S3. Comparison of number of roots per *dz* per tree, $n_{root,i}(z)$ (root m^{-1} $tree^{-1}$), and root projected area with zero azimuth angles per *dz* per tree, $a_{root0,i}(z)$ (m $tree^{-1}$), for (a) our study site for drag measurement (referred to as Bak1 in Yoshikai et al., 2021) and (b) Fukido mangrove forest in Ishigaki Island, Japan (Fuk in Yoshikai et al., 2021). A 0.01-m vertical height interval, *dz*, was used to compute the vertical profiles. Data from 23 trees in Bak1 and 22 trees in Fuk were plotted, respectively.

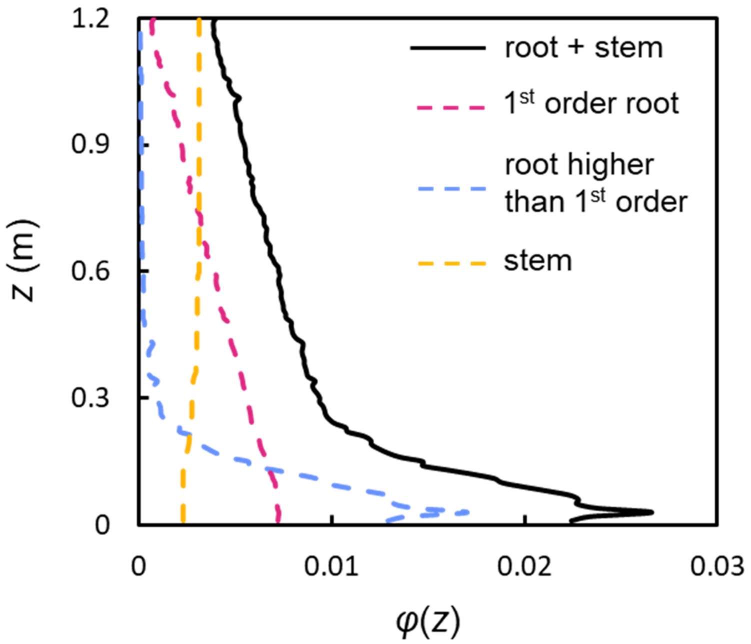

Figure S4. Vertical profile of solid volume fraction (φ, dimensionless), where the values of φ were calculated with 0.01-m vertical resolution. The black solid line shows the solid volume fraction of total vegetation while the red, blue, and yellow dashed lines show the contributions of 1st order root, higher order root, and stem to φ, respectively.